

# TESSERA: Precomputed FAIR Global Pixel Embeddings for Earth Representation and Analysis

Zhengpeng Feng<sup>1</sup>, Clement Atzberger<sup>2</sup>, Sadiq Jaffer<sup>1</sup>,  
Jovana Knezevic<sup>3</sup>, Silja Sormunen<sup>4</sup>, Robin Young<sup>1</sup>,  
Madeline C. Lisaius<sup>1</sup>, Markus Immitzer<sup>2</sup>, Toby Jackson<sup>6</sup>,  
James Ball<sup>3</sup>, David A. Coomes<sup>3</sup>, Anil Madhavapeddy<sup>1</sup>,  
Andrew Blake<sup>5</sup>, Srinivasan Keshav<sup>\*1</sup>

<sup>1</sup>Department of Computer Science and Technology, University of Cambridge.

<sup>2</sup>dClimate Labs.

<sup>3</sup>Department of Plant Sciences, University of Cambridge.

<sup>4</sup>Department of Computer Science, Aalto University.

<sup>5</sup>Clare Hall, University of Cambridge.

<sup>6</sup>School of Biological Sciences, University of Bristol.

Contributing authors: [zf281@cam.ac.uk](mailto:zf281@cam.ac.uk); [clement@cyclops.ai](mailto:clement@cyclops.ai);  
[sj514@cam.ac.uk](mailto:sj514@cam.ac.uk); [jovana.p.knezevic@gmail.com](mailto:jovana.p.knezevic@gmail.com); [silja.sormunen@aalto.fi](mailto:silja.sormunen@aalto.fi);  
[ray25@cam.ac.uk](mailto:ray25@cam.ac.uk); [mcl66@cam.ac.uk](mailto:mcl66@cam.ac.uk); [markus@cyclops.ai](mailto:markus@cyclops.ai);  
[tobydjackson@gmail.com](mailto:tobydjackson@gmail.com); [jgcb3@cam.ac.uk](mailto:jgcb3@cam.ac.uk); [dac18@cam.ac.uk](mailto:dac18@cam.ac.uk);  
[avsm2@cl.cam.ac.uk](mailto:avsm2@cl.cam.ac.uk); [ab@ablake.ai](mailto:ab@ablake.ai); [sk818@cam.ac.uk](mailto:sk818@cam.ac.uk);

**Keywords:** Satellite Remote Sensing, Earth Observation, Foundation Model

Petabytes of satellite Earth Observation (EO) data are freely available and can address critical global challenges. However, EO data quality is poor due to clouds and variable lighting conditions. To address this, practitioners typically use compositing, but this critically removes the temporal phenological signal. Moreover, supervised machine learning to map composited pixels to task-specific classes requires accurately labelled data that are rarely available. We present TESSERA, a pixel-oriented foundation

model for EO time series that creates 128-dimensional latent embeddings requiring only a few labels for task-specific training to achieve state-of-the-art performance across diverse complex tasks. TESSERA uses two encoders that combine optical data with synthetic aperture radar backscatter coefficients at 10m resolution, creating embeddings fused with a multilayer perceptron to generate annual global embedding maps. TESSERA closely matches or outperforms state-of-the-art task-specific models and other foundation models across five diverse downstream tasks. It is unprecedented in ease of use, scale, and accuracy: no other open foundation model provides precomputed outputs with global, annual coverage at 10m resolution.

## 1 Introduction

Monitoring Earth’s dynamic systems through satellite Earth Observation (EO) is critical to addressing global challenges including food security, forest and biodiversity loss, climate change, and disaster mitigation [1–3]. Although petabytes of EO data are available from sensors in various modalities [4], practitioners face fundamental bottlenecks: the scarcity of large, accurately labelled datasets required for supervised training [5], and poor data quality due to sensor noise, cloud cover, atmospheric effects, and non-uniform temporal sampling [6–8].

To mitigate these issues, users typically employ annual or seasonal compositing [9], then apply supervised machine learning to map from composited images to task-specific classification [10]. However, compositing removes the critical temporal signal arising from phenology, and training task-specific ML models is computationally onerous.

Recent EO approaches address the labelling problem using *foundation models*: general-purpose models pre-trained on broad EO datasets [11]. These include supervised pre-training on large labelled datasets [12–15], and self-supervised learning (SSL) strategies that learn from data structure itself. Common SSL techniques include masked autoencoders [16–19], diffusion-based models [20–22], and contrastive methods [23–26]. These foundation models require fine-tuning for specific downstream tasks such as habitat mapping and semantic segmentation [27–31].

Although existing SSL approaches create rich multidimensional embeddings from unlabelled data [32, 33], they still do not address temporal signal loss during compositing. Lisaius et al. [5] demonstrated that the Barlow Twins loss [34], grounded in redundancy reduction principles [35], can preserve spectral-temporal signals in latent embeddings when processing dense EO time series.

Building on this insight, we introduce TESSERA, a pixel-oriented foundation model for EO time series that creates 128-dimensional latent embeddings at 10 m resolution and global scale. TESSERA outperforms state-of-the-art methods across diverse tasks including estimating canopy height in Borneo rainforests, detecting crop types in Austria, mapping above-ground biomass in Finland, identifying fire scars in California and evaluating agroforestry stocking indices in Brazil.

Critically, TESSERA provides precomputed outputs that are fully compliant with FAIR (Findable, Accessible, Interoperable, and Reusable) data principles [36]. The embeddings are findable through a per-tile version-controlled registry, openly

accessible without requiring inference, interoperable via standard numpy arrays and GeoTIFF metadata, and reusable under an open license with fully reproducible model training from open Sentinel-1/2 data. Users need neither fine-tune the model, download voluminous satellite data, nor perform inferencing beyond downstream tasks. This computational frugality, data privacy preservation, and FAIR compliance removes crucial barriers to use. TESSERA is label-efficient, requiring only small numbers of labels for task-specific training to achieve state-of-the-art performance, and is open source for extensibility and reproducibility.

We provide a gap-free, global, annual, 10 m resolution embedding map for 2024 through the GEOTESSERA Python library [37], with plans for global maps covering 2017-2024. We have also released interactive and batch tools for habitat mapping [38].

TESSERA is unprecedented in combining ease of use, scale, and accuracy: no other foundation model provides precomputed outputs while being open and offering global, annual coverage at 10 m resolution using pixel-level spectral-temporal features (Supplementary Text Table 5). The closest work is Google’s AlphaEarth Satellite Embedding foundation model (GSE) [39], which provides similar global coverage but is neither open nor reproducible. We demonstrate that TESSERA embeddings match or outperform AlphaEarth embeddings in several downstream tasks.

## 2 Methods

TESSERA uses self-supervised learning to create per-pixel *embeddings* from a global dataset of unlabelled time-series of observations from Sentinel-1 Synthetic Aperture Radar (SAR) and Sentinel-2 Multispectral Instruments (MSI), learning complementary information from the optical and microwave data streams. It is trained by optimizing a modified Barlow Twins loss function [34]. The original Barlow Twins approach seeks to create embeddings that are a) invariant to *augmentations* of its input, where these augmentations are typically rotations, reflections, and cropping of an image and b) whose dimensions are as decorrelated as possible. Inspired by the work by Lisaius et al. [5], we use the Barlow Twins approach to learn embeddings that are invariant to the choice of random subsets of cloud-free observations in the Sentinel-2 optical time series, fused with the corresponding Sentinel-1 data, while minimizing redundancy between the learned feature dimensions. This is achieved by randomly sampling non-cloudy days from the Sentinel-2 annual observation time series so that model then learns to reconcile these partial views, interpolating missing data.

The loss function includes the standard Barlow Twins terms for invariance and redundancy reduction, complemented with an additional mix-up regularization term to enhance robustness and inter-sample interaction during training (see Supplementary Text Equation 11). We now discuss the system architecture.

TESSERA comprises two main components: a dual-branch encoder and a projector network (see Fig. 1 for details). TESSERA models its input as a set of ‘d-pixels.’ Each d-pixel represents the annual time series of Sentinel-1 and Sentinel-2 observations at a specific 10 m pixel on Earth as a two-dimensional array ordered in time (that is, channels  $\times$  timesteps). This format preserves the temporal evolution of the spectral/backscatter signatures inherent in the satellite data, while allowing observational

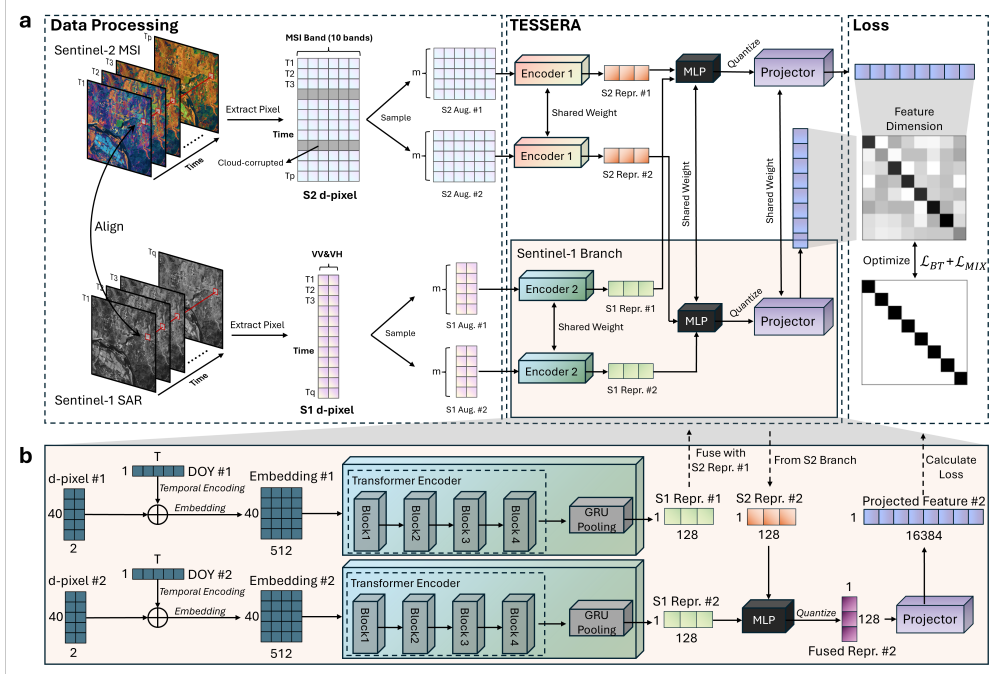


**Fig. 1 Data processing pipeline.** **a**, Overview. Time-series data from Sentinel-2 MSI and Sentinel-1 SAR observations are extracted for each pixel location to form mode-specific ‘d-pixels’ (vertical rectangles; cloud-corrupted rows in gray). Two augmentations are created from each d-pixel as cloud-free random samples from the corresponding d-pixel. Augmentations are processed through a dual-branch architecture with weights shared between the branches. The two resulting 128-dimensional embeddings are fused by a multilayer perceptron (MLP) to create the final output embeddings. During training (but not inferencing) the fused features are expanded to 16,384 dimensions by a large projector network. A modified Barlow Twins loss (a linear combination of  $\mathcal{L}_{BT}$  and  $\mathcal{L}_{MIX}$ ) is calculated from the cross-correlation matrix of projected features, forcing the model to learn dimensionally decorrelated embeddings that are invariant to masked days in the Sentinel-2 d-pixel. **b**, Detailed structure of a single encoder branch. Each d-pixel is embedded using a single-layer MLP (not shown) and a Day-of-Year-based temporal encoding is added. The resulting vector is processed by an 4-block Transformer Encoder and then a Gated Recurrent Unit (GRU) pooling layer; its final hidden state, which summarizes the entire time series, serves as the single 128-dimensional embedding for that modality, which is then passed to the fusion MLP shown in panel **a**.

gaps and irregularities, such as those due to cloud cover or orbit overlap. Rows that are cloud-corrupted or otherwise invalid are indicated by a binary mask and ignored when creating augmentations. Model training and inferencing is done by random temporal sampling followed by flattening of these d-pixels (see Fig. 1 and Supplementary Text for details). In practice, we randomly sub-sample each d-pixel three times, to create a total of three pairs of augmentations. For each 10 m pixel, the fused TESSERA encoders generate a compact (8 bit), 128-dimensional embedding that encapsulates that pixel’s annual temporal and spectral characteristics. Under typical mid-latitude observation conditions, this compresses the input data by a factor of  $\approx 24$ , with higher compression ratios at higher latitudes.

TESSERA uses two separate, parallel Transformer-based encoders: one for Sentinel-1 SAR backscatter data in the C-band (VV and VH polarizations) and another for Sentinel-2 MSI data (10 spectral bands covering the visible, near, and shortwave infrared). Each encoder processes a d-pixel, utilizing multi-head self-attention mechanisms to capture the temporal dependencies and patterns specific to each data modality. Positional encodings derived from the Day-of-Year (DoY) are incorporated to provide temporal context. An attention pooling layer within each encoder aggregates the temporal features into a fixed-size vector that represents the annual signature for that modality [38]. See Figure 1 and Supplementary Text for architectural details.

Modality-specific embeddings derived from dual encoders are fused using a multi-layer perceptron (MLP) which is trained alongside the encoders. This fused embedding, which serves as the 128-dimensional pixel embedding for downstream tasks, is then quantized before being fed into a high-dimensional projector network. This projector, a significantly larger MLP, expands the dimensionality of the fused representation to facilitate redundancy reduction during the self-supervised learning phase. A detailed breakdown of the model’s architectural parameters is provided in the Supplementary table 2.

We have studied how the model’s performance on a typical downstream task improves as we increase the projector dimension (responsible for more than 95% of the model’s parameters) and the amount of computing as well as carried out an ablation study to understand which model components and design decisions are mainly responsible for performance [38].

## 2.1 Model Training

The pre-training phase utilizes a large multi-year global dataset of approximately 800 million d-pixels, down-sampled 400:1 from Sentinel-1 and Sentinel-2 time series from the time period 2017-2024. To ensure successful generalization, a multilevel data sampling, shuffling, and batching strategy was developed. This ensured that each training mini-batch contained a highly diverse set of d-pixels from various geographic locations and acquisition conditions, preventing model overfitting and promoting the learning of universally applicable features. The model was trained for one epoch in this dataset using distributed training techniques (see [38] for further details on data preparation, the shuffling strategy, and optimization). The key hyperparameters used during pre-training are summarized in Supplementary table 4.

## 2.2 Model Inference and Global Embeddings Maps

Following pre-training, the TESSERA dual encoder (with frozen weights and excluding the projector) is used to generate an annual 128-dimensional embedding for every 10 m pixel globally. This involves making inferences from a sample of length 40 from the annual Sentinel-1 and Sentinel-2 time series for each pixel through the trained encoders. To ensure that our maps are gap-free, random sampling with replacement is used to generate augmentations from d-pixels that have fewer than 40 non-cloudy observations. The primary output of this inference stage is a set of annual, global,

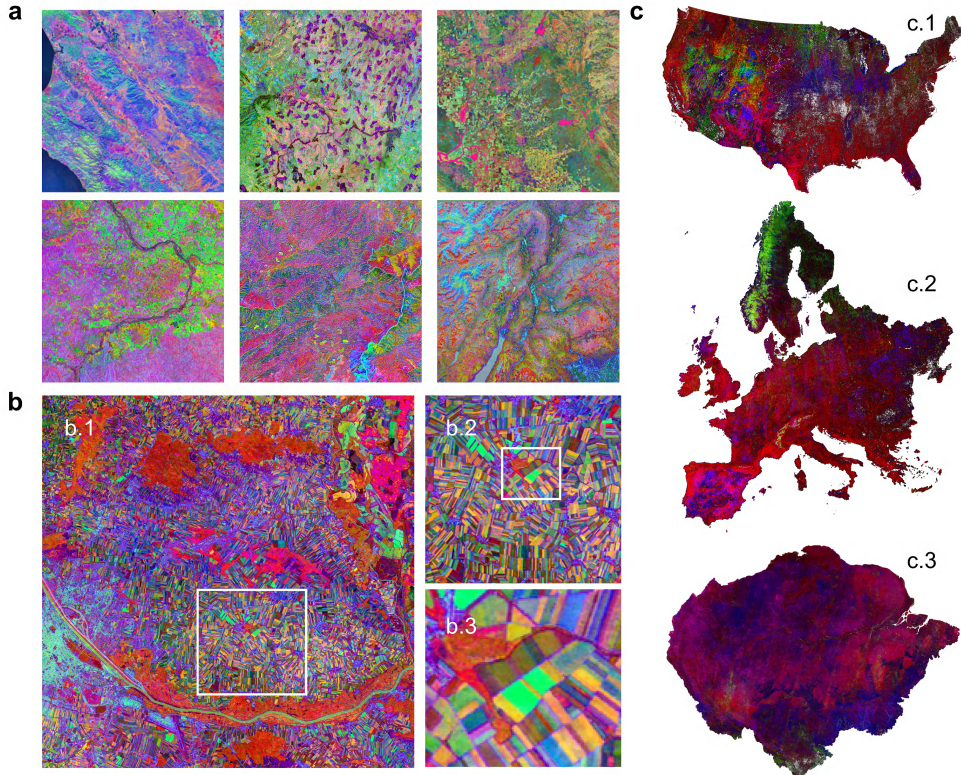


**Fig. 2 TESSERA embeddings capture fine-grained geospatial patterns across multiple scales.** The first three dimensions of the 128-dimensional embeddings are mapped to RGB channels for visualization. **a**, Examples from diverse global locations, showing a variety of landforms and vegetation patterns. **b**, A multi-scale view of a complex agricultural landscape. **b.1** shows the overall region, with subsequent panels (**b.2**, **b.3**) zooming into the white-boxed areas, revealing progressively finer details down to individual crop fields. **c**, Continental-scale visualizations demonstrating the richness and consistency of the embeddings over vast areas, including (**c.1**) the Continental United States, (**c.2**) Europe, and (**c.3**) the Amazon basin.

10 m resolution TESSERA embedding maps. These maps are designed as readily usable multichannel geospatial data layers. This “Embeddings-as-Data” approach significantly lowers the barrier to entry for end-users, as these rich, precomputed features can be directly ingested by downstream models without the need for raw satellite data processing or running the TESSERA model itself (see Supplementary Text). We are currently generating global embeddings for 2024 (approx. 250 TB) and will progressively extend coverage backward year by year until 2017. Visualizing the first three dimensions of the embeddings as R, G, and B channels reveals rich, detailed textures corresponding to diverse land cover and land use patterns. These visualizations highlight the model’s ability to capture information across multiple scales, from individual agricultural fields to entire continents (Fig. 2).

### 3 Downstream Tasks

The effectiveness and generalizability of the TESSERA embeddings are evaluated on a diverse range of downstream remote sensing tasks. These include pixel-wise classification, such as for crop type mapping, pixel-wise regression, such as for estimating canopy height and carbon density of forests, and patch-based dense predictions, such as for semantic segmentation. (See Supplementary fig. 12 for the general downstream application workflow.) In these evaluations, the pre-trained TESSERA encoder, with frozen weights, acts as a feature extractor (although, given adequate computing resources, fine-tuning the model is also possible), converting d-pixels from a region of interest to embeddings. Lightweight, task-specific model heads (e.g., shallow MLPs or UNet-style decoders) are then trained using these embeddings, acting as explanatory variables in regression modelling. This approach is computation- and labelled-data efficient: it typically requires substantially less labelled data and computational resources compared to training deep models from scratch, yet achieves or surpasses the state-of-the-art.

#### 3.1 Crop Type Classification

Agricultural monitoring through EO is a cornerstone of managing global food security, providing critical data to stakeholders in the agricultural sector [40]. The classification of crop types informs vital agricultural decisions by allowing accurate estimates of crop area and production, and facilitating low-cost monitoring of diseases and pests in vast regions [7]. However, this task is considerably more complex than many other challenges in the classification of land cover, as it requires discerning subtle spectral and temporal variations that differentiate different crop classes [7]. In the past, classifiers such as Random Forest (RF) applied to hand-crafted composite time series data have established the standard [7, 41]. Recent advances have shifted towards foundation models, which, unlike bespoke machine learning models that require region-specific feature extraction and training, offer generalizable representations that can be applied universally [42, 43]. Here, we demonstrate that TESSERA’s precomputed embeddings set a new state-of-the-art.

To evaluate performance, we used the INVEKOS Austrian crop dataset [44] from the 2021–2022 growing season. This is an extensive data set that covers 1850 km<sup>2</sup> east of Vienna with 154 different crop types, which we consolidated into 17 classes based on crop similarity (e.g., merging feed beet with sugar beets) [44]. We compared the performance of a small classifier neural network trained using TESSERA embeddings with three key state-of-the-art alternatives: (1) an RF classifier trained on engineered temporal features from raw satellite data, (2) the PRESTO foundation model [19], and (3) Google AlphaEarth Satellite Embedding (GSE) [39]. For the foundation models, we used the same small neural network to classify their respective embeddings to allow a direct comparison. We evaluated performance using multiple metrics, including F1 scores, under varying data availability scenarios, from 30% of labelled data to one-shot learning. We also evaluated performance on a patch-based semantic segmentation task against several other foundation models. Details on data processing, model architectures, and training protocols are provided in the Supplementary Text.

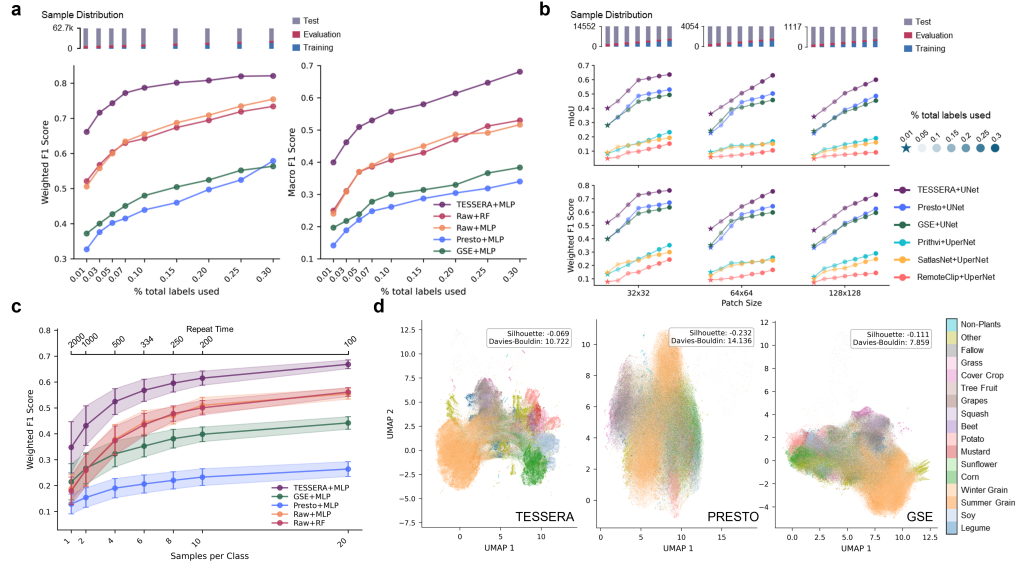


**Fig. 3 TESSERA embeddings achieve state-of-the-art performance in crop type classification.** The evaluation was conducted on the 2022 Austrian crop dataset. **a**, Weighted and Macro F1 scores for pixel-wise classification as a function of the training data ratio. TESSERA embeddings, coupled with a simple MLP, consistently outperform a Random Forest model and other foundation models like PRESTO and Google AlphaEarth Satellite Embedding (GSE). **b**, Patch-based semantic segmentation performance comparison. TESSERA embeddings, used with a UNet model, achieve higher mean Intersection over Union (mIoU) and Macro F1 scores than other foundation models across various patch sizes and training data ratios. **c**, Weighted F1 score in few-shot learning scenarios. TESSERA maintains a significant performance advantage even with very few training samples per class. Error bars represent the standard deviation over multiple runs. **d**, UMAP visualization of the embedding spaces for TESSERA, PRESTO, and GSE for 17 crop classes. TESSERA’s embeddings exhibit clearer separation and more coherent clustering visually.

TESSERA consistently surpasses both baselines in all training regimes, especially in settings where labelled data are scarce (Fig. 3). In pixel-wise classification tasks with training data splits from 1% to 30%, a simple MLP trained on TESSERA embeddings achieves higher weighted and macro F1 scores than an identical MLP trained on PRESTO or GSE embeddings, and substantially outperforms the RF baseline (Fig. 3a). TESSERA also maintains statistically significant advantages in one-shot and few-shot scenarios (Fig. 3c). Furthermore, TESSERA’s utility extends to patch-based semantic segmentation, where it consistently achieves higher mIoU and macro F1 scores compared to other leading foundation models, including PRESTO and GSE, across various patch sizes (Fig. 3b).

These performance gains are due to the high quality of the learned embeddings. A UMAP analysis [45] of the embedding space reveals that TESSERA embeddings form tighter, more semantically coherent clusters by crop class compared to those from PRESTO and GSE (Fig. 3d). This improved separability highlights the strength of TESSERA as a foundational tool for agricultural applications.

### 3.2 Canopy Height Estimation

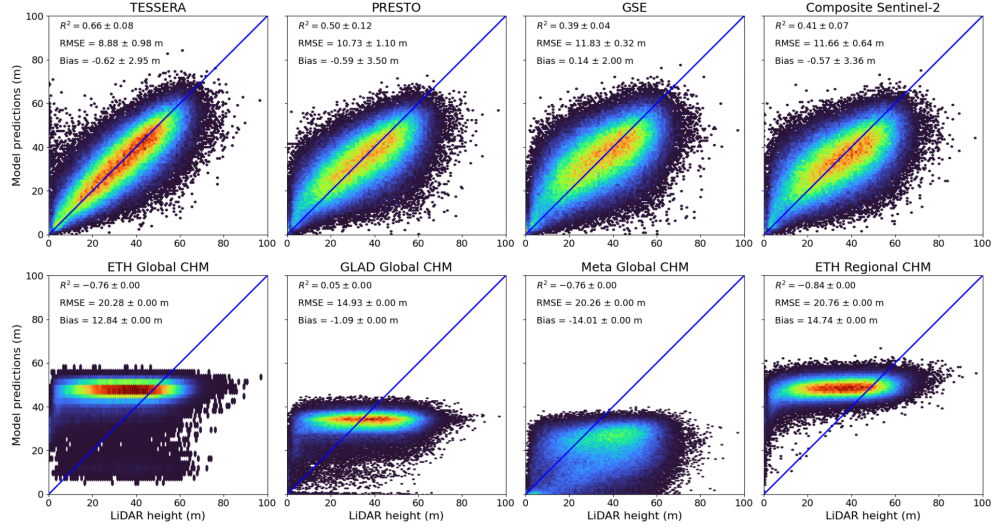


**Fig. 4 TESSERA outperforms global and regional models as well as alternative pixel-based foundation models in canopy height estimation.** Predicted canopy height (y-axis) is compared against airborne LiDAR reference data (x-axis) across multiple models and input datasets in Danum Valley, Borneo. **Top row:** Predictions from models trained using different input representations—TESSERA, PRESTO, Google AlphaEarth Satellite Embedding (GSE), and raw Sentinel-2 composites—using the same model architecture and training procedure. TESSERA achieves the highest coefficient of determination and the lowest RMSE ( $8.88 \pm 0.98$  m), indicating superior performance in structurally complex, tall tropical canopies. **Bottom row:** Comparisons to existing global and regional canopy height maps, including products from ETH, GLAD, Meta, and Lang et al.’s regional CHM. All four products show substantially lower predictive performance ( $R^2 < 0.05$ ,  $RMSE > 14$  m), with three exhibiting negative correlations. These models saturate at lower canopy heights and show large bias and RMSE, highlighting the limitations of global products when applied to high-biomass tropical forests without local calibration. A 1:1 reference line (blue) is shown in each panel for comparison.

Canopy height is a key structural attribute of forests, linked to above-ground biomass and carbon stocks, and therefore important for climate mitigation efforts and carbon accounting frameworks such as REDD+ [46, 47]. It is correlated with ecosystem function [48], forest age, and successional stage, while also serving as a proxy for habitat quality, an important determinant of biodiversity patterns and species richness [49–51]. Accurate, scalable canopy height models (CHMs) can enable detection of forest degradation and disturbance.

Despite substantial progress in global canopy height mapping, current approaches exhibit limitations that restrict their reliability and applicability. Airborne Laser Scanning (ALS), where laser-based LiDAR instruments are carried in an aircraft flying over a target region, creates highly accurate benchmark datasets, but is necessarily restricted in geographical range [52]. GEDI, a spaceborne LiDAR system, can provide

accurate point measurements of canopy height to train models to map canopy height from optical and radar data; however, it does not provide wall-to-wall maps, does not sample high latitudes [53], and does not produce unreliable estimates in mountainous terrain [54]. Radar-based CHMs (e.g., TanDEM-X) achieve global coverage, but are affected by canopy height saturation in dense forests and depend on high-quality terrain models to accurately isolate canopy height [55]. Optical data, while widely available, may lack inherent sensitivity to vertical structure and require indirect proxies or fusion with information from active sensors [56, 57] - yet none of the three most widely used global CHM models currently implement sensor fusion [58–60]. Most approaches instead rely on a single sensor type and derive height predictions either from temporal composites or from large numbers of hand-engineered features (e.g., > 500 features in Potapov et al. [59]), which may generalize poorly across ecosystems. These models tend to underestimate tall canopies, especially in tropical forests where most of the above-ground carbon is stored, and face challenges from persistent cloud cover, sensor saturation [61], and inconsistencies in input quality. As a result, significant discrepancies remain between global CHMs and ALS benchmarks, and current products underestimate local variability and structural extremes [62]. Most CHMs are also static, failing to capture inter-annual dynamics, and inconsistencies in methodology and sensor characteristics hinder cross-product integration. These limitations underscore the need for scalable, temporally resolved, and sensor-fused CHMs with quantified uncertainties to support forest monitoring, carbon accounting, and Earth system modelling [63, 64].

We evaluated TESSERA embeddings to predict canopy height at 10 m resolution within a  $5 \times 6$  km area of tall old-growth tropical forests in the Danum Valley, Borneo [65] with openly available ground-truth data [66]. To ensure spatial independence, we conducted four-fold spatial cross-validation against the airborne LiDAR-derived canopy height, each time holding out a contiguous 50% of the region for testing and using the remaining 50% for training and validation. A 30-million-parameter UNet was trained using  $32 \times 32$  pixel patches of the embeddings as input. To account for variability in training convergence, we performed three independent training runs per fold, each for 200 epochs, and retained the model with the best performance on the validation set. The accuracy metrics for the foundation models are reported as the average across the 12 runs. TESSERA achieved a coefficient of determination ( $R^2$ ) of 0.66, a root mean squared error (RMSE) of 8.88 m, and a mean bias of  $-0.62$  m.

We benchmarked TESSERA’s performance against state-of-the-art approaches through three sets of comparisons (Fig. 4). First, we evaluated its predictions against three global canopy height products: the GLAD map by Potapov et al. [59], the ETH map by Lang et al. [58], and the Meta map by Tolan et al. [60]. Although local regression models, such as ours, generally outperform global products in regional evaluations [67], the pronounced saturation of these global models at much lower canopy heights—combined with RMSEs that exceed their reported global averages [58–60]—underscores the challenge of accurately mapping structurally complex high canopy regions such as Danum Valley.

We also compared our results with regional wall-to-wall canopy height maps for Indonesia, Malaysia, and the Philippines produced by Lang et al. [68], which used deep convolutional neural networks trained in Sentinel-2 time series and GEDI LiDAR to

estimate the regional canopy height and biomass. Second, we compared TESSERA to two alternative pixel-based foundation models, PRESTO [19] and Google AlphaEarth Satellite Embedding (GSE) [39], using the same U-Net architecture, but replacing TESSERA’s input representations with those of the other foundation models. Finally, to assess the added value of the learned representations over the raw input data, we trained the same U-Net using cloud-free annual median composites of Sentinel-2 imagery.

In all comparisons, TESSERA outperformed competing methods. Moreover, its embeddings do not require pre-processing, greatly enhancing reproducibility. Instead, only the region and year of interest are needed to replicate the input data pipeline. By fusing Sentinel-1 and Sentinel-2 data without requiring preprocessing or careful selection of input features, TESSERA’s 128-dimensional embeddings encode cloud-free, information-rich signals that effectively address key challenges in canopy height modelling.

### 3.3 Above-ground Forest Biomass Estimation

Forests play a central role in the global carbon cycle [69]. This motivates the need for reliable and scalable above-ground biomass (AGB) estimates of forest carbon stocks to allow monitoring of deforestation, forest degradation, and forest recovery [70]. A critical problem in AGB estimation is that, as with canopy height estimation, precise values are best obtained from field plots or airborne laser scanning, which are too costly to scale beyond small geographic regions. Thus, there has been a long-standing effort to link field measurements to global satellite observations [71].

Recently, with the creation of the BioMassters benchmark dataset [72] (more on this below), a global challenge was issued to research groups to predict AGB in Finnish forest patches from Sentinel-1 and Sentinel-2 satellite observations using a machine learning approach of their choice [73]. We found that the winner, chosen from more than 1,000 submissions, achieved a mean RMSE value of 25.93 tonnes/hectare (t/ha), a substantial improvement over the prior benchmark score of 101.98. In our work, we compared a regression model trained on TESSERA embeddings with this winning model, as well as regression models trained on embeddings from two other foundation models: SpectralGPT [18] and GSE [39].

First, a summary of the BioMassters dataset. This data set contains 11,462 patches of Finnish forests from 2017 to 2021, with associated ground truth AGB values provided by the Finnish Forest Center and the National Land Survey derived from airborne LiDAR scanning (ALS), aerial imagery and calibrated allometric equations [74, 75] informed by extensive field plots. Each patch covers a  $2560 \times 2560 \text{ m}^2$  area, with a spatial resolution of 10 m per pixel. The fine spatial granularity of the dataset makes the estimation task more challenging, as it introduces a long, thin tail of high AGB values (Fig. 5b) that would not appear in coarser resolution data. To reduce the influence of implausibly high AGB values, we clip values above 500 t/ha to this threshold.

We compared a UNet-based regression model [76] trained on TESSERA embeddings with SpectralGPT embeddings [18] combined with a lightweight spatial-temporal encoder [77] for temporal aggregation and a UPerNet [78] regression head, because

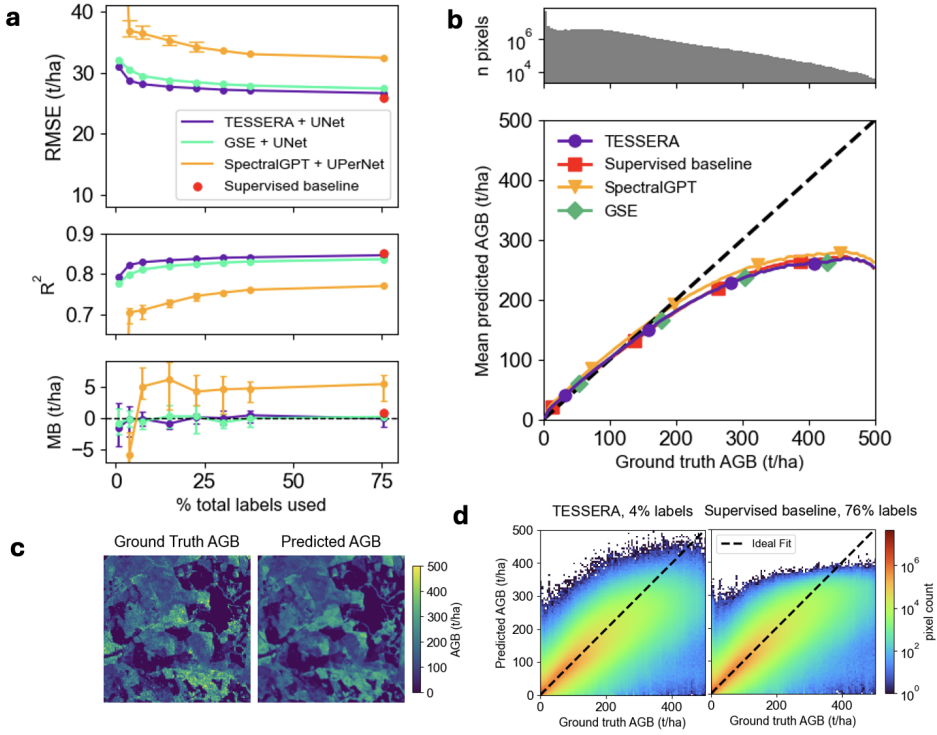


**Fig. 5** A regressor trained on TESSERA embeddings matches the performance of winner of the BioMassters competition with far fewer labels, outperforms SpectralGPT+UPerNet, the best performing foundation model in the BioMassters challenge, and matches the performance of the commercially-developed GSE embeddings. **a**, TESSERA achieves lower RMSE values than SpectralGPT+UPerNet and results similar to the state-of-the-art supervised baseline and Google Satellite Embedding foundation model (top row). The coefficient of determination ( $R^2$ ) and mean bias (MB) are shown in the middle and bottom row as functions of label availability. **b**, Mean predicted AGB values show increasing bias at higher ground-truth AGB values, which, however, are sparse in the dataset (the y-axis in the upper panel is on a logarithmic scale). Mean predictions are calculated for ground-truth AGB values grouped into 5 t/ha intervals. **c**, Predicted AGB map for an example patch using 4% of labels in training. **d**, Pixel-wise comparison of predicted versus ground-truth AGB values for the test data with TESSERA+UNet (left) and the supervised baseline (right). The supervised baseline ignores ground-truth values above 400 t/ha during training, which is reflected in its lower maximum predictions.

this combination has been found in the Pangaea benchmark [79] to outperform other foundation models [72, 79]. Unfortunately, as of the time of this writing, SpectralGPT's preprocessing pipeline has not yet been published in their codebase. Thus, we adopted the Pangaea implementation of their model [79], which uses preprocessed satellite imagery from the BioMassters dataset. We also compared TESSERA with the model that won the BioMassters competition as our state-of-the-art supervised baseline. This model uses a UNet with a temporal attention encoder [72]. Our comparison

of TESSERA to the supervised baseline and SpectralGPT is not entirely straightforward, as the snapshot satellite data used in these models differs from the annual time series required as TESSERA’s input. However, these discrepancies can be considered as an inherent part of the respective processing pipelines and hence largely unavoidable. Finally, we compared our work with a UNet-based regressor trained on GSE embeddings.

Our performance metrics are the mean RMSE, the coefficient of determination ( $R^2$ ), and the mean bias (MB) in AGB across the test patches as a function of the fraction of labelled data used to train the regressor (Fig. 5a). We make three significant findings. First, although custom models developed using supervised learning are typically difficult to outperform, even with a small fraction of training labels, our regressor nearly matches the performance of the BioMassters competition winner, which uses a supervised learning approach. Second, our regressor trained on 1% of the labelled data outperforms a UPerNet-based regressor trained on the entire training set using SpectralGPT embeddings. Third, our regressor achieves performance comparable to GSE, a commercially developed foundation model with far more training resources at its disposal.

### 3.4 Burned Area Detection

The frequency and severity of wildfires are projected to increase in many parts of the world due to climate change [80–82]. Accurate maps of burned areas and burn severity are critical for monitoring wildfire trends [83], predicting wildfire occurrence [84], assessing ecosystem recovery [85], and establishing effective fire management strategies [86].

Remote sensing is widely used to detect burned areas and assess severity regionally and globally [87]. Most existing burn area mapping approaches rely on time-series analysis or direct comparison between pre-fire and post-fire images, often requiring careful selection of suitable cloud-free images, manually tuned thresholds, and expert input [87, 88]. These methods typically use spectral indices such as the Normalized Burn Ratio (NBR), although many studies have also explored the design of custom features and applied spectral dimensionality reduction techniques to preserve key fire-related signals [87]. Most existing methods use optical sensors [87], which can detect fire-specific spectral signatures but are susceptible to cloud cover [89], particularly problematic for fire detection in ecosystems where vegetation rapidly re-greens [90]. SAR offers complementary sensitivity to vegetation structure and is unaffected by cloud cover [87, 91, 92]. Recent reviews emphasize the need for multimodal remote sensing, combining passive and active sensors to improve accuracy and robustness [87, 93]. Sentinel-1 and -2 sensors in particular, when combined together at 10 m resolution, have shown promise in detecting burn areas from small fires that are often left out of coarse, global burn area products [91, 92, 94]. TESSERA extends these approaches by encoding temporal dynamics, while addressing major limitations through the use of multimodal sensors and the use of data-driven features learned directly from large volumes of combined Sentinel-1 and Sentinel-2 time series (Fig. 6).

We tested whether TESSERA embeddings capture fire-induced disturbance by evaluating their ability to detect burned areas and severity of the burn (Fig. 6). Our

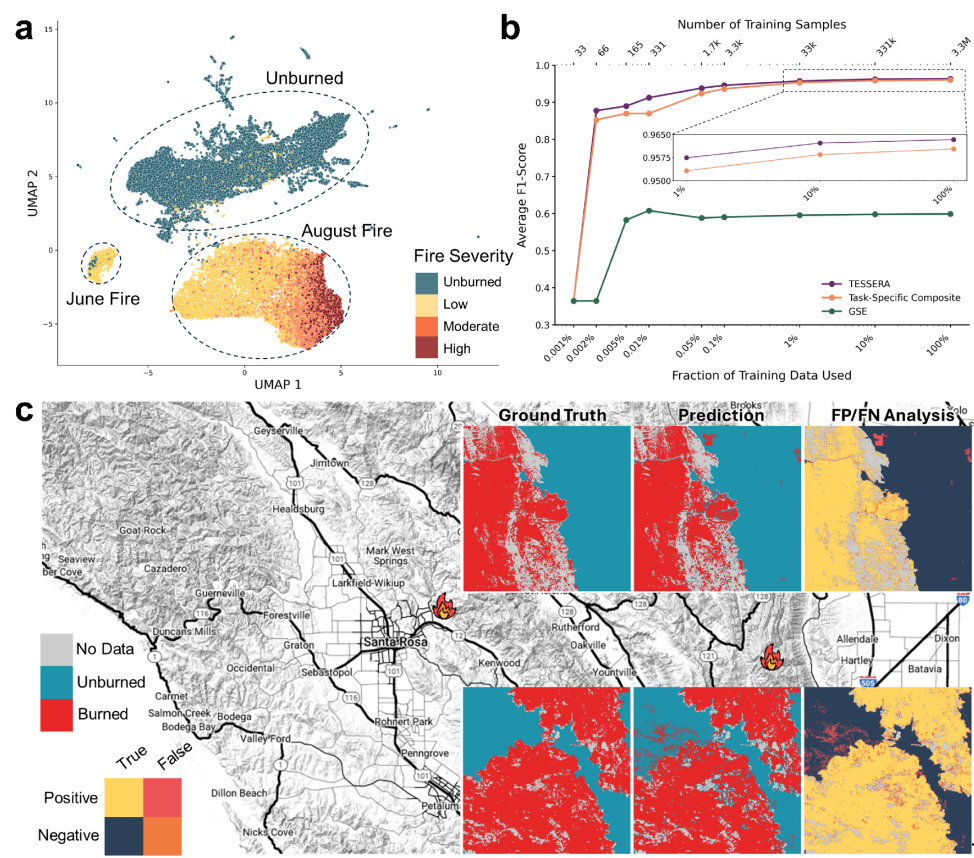


**Fig. 6** Fire disturbance detection using TESSERA embeddings across two burned regions in California. **a**, UMAP projection of 2020 TESSERA embeddings reveals clear structure separating unburned pixels and two temporally distinct fire events. A continuous gradient within the August fire aligns with MTBS burn severity classes, suggesting that TESSERA captures both timing and magnitude of disturbance. **b**, Burned vs. unburned classification performance using random forest classifiers trained on different input representations. TESSERA achieves high F1-scores with minimal training data and performs comparably to a task-specific composite baseline, while significantly outperforming Google AlphaEarth Satellite Embeddings (GSE). **c**, Burn classification maps generated from models trained on 1% of labelled data demonstrate strong agreement with MTBS perimeters across both test areas. As MTBS is itself derived from remote sensing imagery, discrepancies may reflect methodological differences rather than prediction error.

analysis focused on two randomly selected  $15 \times 15$  km regions in California that experienced wildfires in 2020, using fire boundaries and burn severity labels from the Monitoring Trends in Burn Severity (MTBS) dataset [95]. UMAP projections [45] of the TESSERA embeddings revealed a strong separability between burned and unburned pixels, with individual fires forming distinct clusters. In particular, a gradient in the UMAP space was aligned with the severity of the burn in both areas, indicating that TESSERA encodes not only the occurrence but also the magnitude

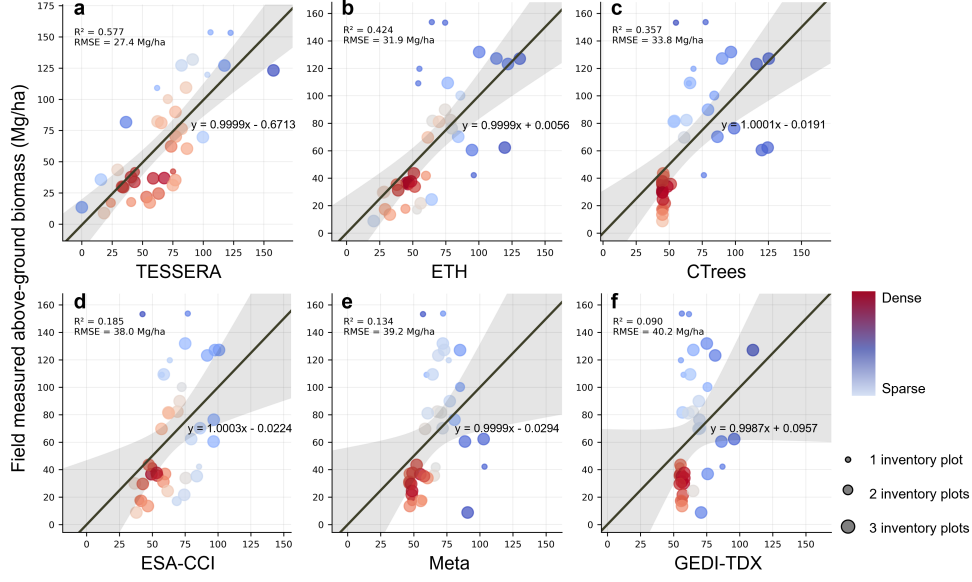


**Fig. 7 TESSERA outperforms various stocking indices commonly used in the Voluntary Carbon Market (data has been linearly rescaled).** Comparison of in-situ AGB measurements in 38 agro-forestry sites, within which 1-3 inventory plots were measured in Para State, Brazil with TESSERA (top left) and five other remote sensing products. Note that the different products were originally provided in different units and converted to AGB (see [38] for details).

of the disturbance (Fig. 6a). To quantify separability, we trained a Random Forest classifier to distinguish burned pixels from unburned pixels. We compared three input representations: (1) TESSERA embeddings, (2) Google AlphaEarth Satellite Embeddings (GSE), and (3) a task-specific baseline constructed from pre- and post- fire Sentinel-2 composites. The classifier trained in TESSERA embeddings achieved an average F1 score of more than 0.96 (Fig. 6b). Remarkably, it reached over 90% of its final performance using only 0.01% of the training labels ( 330 pixels), demonstrating strong data efficiency. These results show that TESSERA’s annual task-agnostic embeddings perform on par with a task-specific baseline that requires prior knowledge of fire timing and spectral properties, while significantly outperforming other commercially developed foundation models such as Google Satellite Embeddings.

To assess practical utility, we used models trained in 1% of the data to generate wall-to-wall burn maps. These predictions closely matched MTBS perimeters and exhibited minimal false positives in the unburned areas (Fig. 6c). The results confirm that TESSERA’s general-purpose representations encode high-resolution disturbance signatures and support efficient, scalable fire mapping workflows without relying on handcrafted features or task-specific adjustments.

### 3.5 Stocking Indices in Voluntary Carbon Markets

The conversion of degraded pastures into species-rich agroforestry systems has the potential to increase carbon sequestration without displacing cattle grazing activities elsewhere [96]. To fund the transition, project developers can participate in the voluntary carbon market (VCM), but need to monitor above-ground biomass (AGB) over potentially large areas. This is a costly and inefficient undertaking if it is done only by field sampling.

To enable cost reductions, the most widely applied standard in the VCM (VM00047 from Verra [97]) allows project promoters to use remotely quantified 'stocking indices' to assess project performance between 5-yearly ground truth assessments; project developers need to demonstrate that the chosen stocking index is correlated with the AGB. Upon acceptance, project developers can use the index to assess the performance of the project. Here, we evaluate a simple TESSERA-derived stocking index against five widely used globally-available canopy height and AGB products that are often used in the VCM. To derive the stocking index from the TESSERA embeddings, GEDI relative height differences between RH95 and RH10 were used as target values for a pixel-wise random forest regression following the methodology outlined in Atzberger et al. [98]. Without further fine-tuning, the derived stocking index, as well as five other state-of-the-art canopy height and AGB products (see [38] for details), were individually rescaled so that their regression lines best matched (i.e., with slope 1 and zero bias) *in situ* data collected at 38 agroforestry sites in Para State, Brazil. This rescaling ensures a fair comparison between the various products.

A comparison of R<sup>2</sup> and RMSE demonstrates that the TESSERA-derived stocking index consistently outperforms alternative products (Fig. 7). As the alternative stocking indices all use similar (optical and microwave) inputs to derive canopy height, respectively, AGB, the superior performance of the TESSERA-derived stocking index must be attributed to the efficiency of the TESSERA embeddings.

## 4 Conclusion

In this work, we introduce TESSERA, an innovative remote sensing foundation model that provides ready-to-use embeddings with worldwide coverage at 10 m resolution through self-supervised learning applied to pixel-level optical and microwave satellite time series data. TESSERA embeddings establish new performance standards, while our open-source methodology, FAIR-compliant data distribution through version-controlled registries, standard geospatial formats, and the GEOTESSERA library permit reproducible science and enable use of our work even by non-specialists who lack access to high-performance computing. We evaluated TESSERA's capabilities across five distinct tasks, benchmarking our approach against leading task-specific models and existing foundation models. Our findings demonstrate that TESSERA surpasses both conventional RF baselines and current state-of-the-art geospatial foundation models in these diverse downstream applications.

## 5 Acknowledgments

We gratefully acknowledge support from Mantle Labs and help from AMD Inc., Tarides, Jane Street, the Dawn supercomputing team at Cambridge, the Aalto University Science-IT project and the Aalto Scientific Computing team, and the UKRI STFC AIRR Programme for providing us access to compute resources.

### ***Funding:***

ZF and SK were funded by a charitable donation made by Dr Robert Sansom to the University of Cambridge. SJ was funded by a charitable donation from John Bernstein. JB received support from the UKRI CRCRM scheme (grant MR/Y024354). SS received funding from the Jenny and Antti Wihuri Foundation and the Helsinki Institute for Information Technology. DAC and SK were funded by the NERC Centre for Landscape Regeneration (NE/W00495X/1). TJ was funded by NERC grant NE/S010750/1. MCL was funded by UKRI and Mantle Labs.

### ***Author contributions:***

Initial conceptualization: CA

System design: CA, ZF, SJ, SK

System implementation: ZF, RY, MCL, AM

Data collection: TJ

Data analysis: ZF, RY, JK, SJ, AM, TJ, DAC, SK

Downstream tasks: MCL, CA, SS, DAC, CA, MI, ZF, JK

Paper conceptualization: SK, AM, DAC, AB, SJ

Paper draft: ZF, MCL, RY, SS, SK, JK

Paper review and refinement: All

### ***Competing interests:***

There are no competing interests to declare.

### ***Data and materials availability:***

Our framework integrates openly available data from the Copernicus Sentinel-2 (S2) [99] optical and Sentinel-1 (S1) [100] SAR missions, leveraging the strengths of each sensor. We used S2 Level-2A surface reflectance products, providing detailed spectral information across 10 bands (Red, Blue, Green, NIR, NIR8, Red-edge1, Red-edge2, Red-edge3, SWIR16, and SWIR22). To remove cloud contamination, we filtered the time series using the associated Sen2Cor scene classification map to mask cloudy observations. For SAR data, we processed Sentinel-1 Ground Range Detected imagery to derive calibrated backscatter coefficients in VV and VH polarizations, applying standard corrections using the ESA SNAP toolbox [101].

The Google Satellite Embedding V1 dataset [39] is licensed under CC-BY 4.0 and is produced by Google and Google DeepMind.

PRESTO embeddings can be created on demand in Google Earth Engine [102] using VertexAI [103].

Our global embedding map—initially for 2024 and eventually one for each year from 2017 to 2024—is  $\sim 250$  TB and is freely available for download, along with the parameters of the TESSERA model, the code to retrieve Sentinel-1 and Sentinel-2 data, and the training and inferencing code [37]. To allow for the seamless use of our embeddings in existing geospatial workflows, we have released the GEOTESSERA Python library into the PyPI repository [104], which is the official third-party software repository for Python. This library automates the retrieval of TESSERA embeddings for a given year and geographical region, merging them into a numpy buffer [105] that can be passed directly into downstream tasks. The embeddings are indexed using Pooch [106] with per-tile checksums stored in an open Git repository, allowing users to pin specific versions for reproducibility or automatically refresh to the latest embeddings as needed. Additionally, a Parquet index is published daily for rapid spatial queries across the entire dataset.

The crop type identification downstream task uses the open INVEKOS Austrian crop dataset [44].

The burn area detection task uses the open Monitoring Trends in Burn Severity (MTBS) dataset [95].

The canopy height downstream task uses open access airborne laser scan data collected in the Danum valley and Sepilok [66].

The AGB downstream task uses the open BioMassters dataset [72]. The code for the winning model of the BioMassters competition is described in [72] and freely available on the corresponding GitHub page.

The implementation of SpectralGPT+UPerNet model is available in the Pangaea benchmark [79].

The stocking index downstream task uses plot data from 38 plots in Brazil. This contains private information regarding plot owners; hence, data access will require a Data Transfer Agreement.

## A Materials and Methods

**Table 1** Variable definitions for remote sensing data structure

Variable	Dimensions	Description
$R_t$	$W \times H \times C$	Remote sensing data tile at time $t$
$V_t$	$W \times H$	Binary mask for tile at time $t$ (1=valid, 0=invalid/clouded)
$\mathbf{D}$	$T \times W \times H \times C$	Complete temporal data stack
$\mathbf{M}$	$T \times W \times H$	Complete temporal mask stack
$S_{i,j,c}$	$T \times 1$	Time series for channel $c$ at location $(i,j)$
$P_{i,j}$	$C \times T$	d-pixel: all spectral channels by timesteps at location $(i,j)$
$m_{i,j}$	$T \times 1$	d-pixel mask indicating valid timesteps at location $(i,j)$
$W, H$	Scalar	Spatial dimensions (width, height)
$C$	Scalar	Number of spectral channels + polarizations
$T$	Scalar	Number of time steps

## A.1 Model details

Our input data consists of Sentinel-2 optical satellite imagery (Level-2A bottom-of-atmosphere) and Sentinel-1 Synthetic Aperture Radar (SAR, Radiometrically Terrain Corrected).

### *Data Representation*

We consider remote sensing data [99, 100] with  $C$  channels (spectral bands or polarizations). Each data tile  $R_t$  at time  $t$  is represented as a 3D array with dimensions:

$$R_t \in \mathbb{R}^{W \times H \times C} \quad (1)$$

where  $W$  is the width (longitude dimension),  $H$  is the height (latitude dimension), and  $C$  is the number of spectral channels.

Each tile is accompanied by a corresponding binary mask  $V_t$  of dimensions:

$$V_t \in \{0, 1\}^{W \times H} \quad (2)$$

where  $V_t(i, j) = 0$  indicates clouding or missing data for the pixel at spatial coordinates  $(i, j)$ , and  $V_t(i, j) = 1$  indicates valid data.

### *Temporal Data Stacking*

We stack spatially aligned tiles over a time period that spans  $T$  time steps ( $t = 0, 1, \dots, T - 1$ ). The temporal data stack is defined as:

$$\mathbf{D} = [R_0, R_1, \dots, R_{T-1}] \quad (3)$$

$$\mathbf{M} = [V_0, V_1, \dots, V_{T-1}] \quad (4)$$

### *Time Series Extraction and d-pixel Definition*

For a given spatial location  $(i, j)$  and spectral channel  $c$ , the time series  $S_{i,j,c}$  represents all channel  $c$  values at coordinates  $(i, j)$  over the entire time period:

$$S_{i,j,c} = [R_0(i, j, c), R_1(i, j, c), \dots, R_{T-1}(i, j, c)] \quad (5)$$

We define a *d-pixel*  $P_{i,j}$  as the collection of all spectral channels by timesteps at a given spatial location  $(i, j)$ :

$$P_{i,j}(c) = S(i, j, c) \quad (6)$$

In other words, the d-pixel provides all spectral values (Sentinel-2) or backscatter values (Sentinel-1) at a given point over time. Note that d-pixels can be sparse and are accompanied by a mask vector  $m_{i,j}$  of size  $T$  that indicates the timesteps for which there are valid data, with a value 1 indicating that the corresponding row in  $P_{i,j}$  is valid.

### *The d-pixel Representation*

We represent each 10 m pixel in the time series of images from annual multispectral (Sentinel-2) and SAR backscatter (Sentinel-1) as a “d-pixel” array (see Fig. 1 a). In this array, each row corresponds to a chronologically ordered observation date, and each column is a specific spectral band or polarization. This representation accommodates data gaps encountered in remote sensing due to cloud cover (for optical data) or other atmospheric interference and acquisition irregularities. Observations identified as invalid (e.g., via Sentinel-2 scene classification layers for clouds, or missing Sentinel-1 acquisitions) are masked and are handled by downstream model components, for instance, by being ignored in the temporal sampling process.

### *Dual-Encoder Architecture*

Given the distinct nature of Sentinel-1 SAR and Sentinel-2 MSI data, TESSERA employs two separate, parallel transformer-based encoder branches.

- **Sentinel-2 MSI Encoder:** This branch processes a time series of 10 spectral bands (excluding the 60 m bands used for the detection of water vapour and clouds) from Sentinel-2. We used blue (B2), green (B3), red (B4), red edges 1–3 (B5, B6, B7), near-infrared (B8, B8A), and shortwave infrared (B11, B12).
- **Sentinel-1 SAR Encoder:** This branch processes a time series of 2 polarizations from Sentinel-1 (VV and VH).

Each encoder begins by linearly embedding the input features (spectral bands or polarizations) for each time step. To preserve sequence order and incorporate temporal context, learnable positional encodings based on the Day-of-Year (DOY) of each observation are added to these embeddings. The core of each encoder consists of a stack of 4 standard Transformer blocks [107], featuring multi-head self-attention and feed-forward layers to learn temporal patterns within the data streams.

To derive a single vector summarizing the entire time series for each modality, an attention-pooling layer weighs the importance of different time steps before aggregation. The resulting modality-specific embeddings (one from the S1 encoder, one from the S2 encoder) are then fused using a multi-layer perceptron.

### *Projector Network*

The fused embedding from the dual-encoder stage is subsequently fed into a large projector network. This projector is a six-layer MLP. Its architecture comprises an input layer mapping the fused embeddings to 16,384 dimensions, followed by four hidden layers of 16,384 dimensions each, and a final linear output layer. Each of the first five layers is a fully-connected linear layer followed by Batch Normalization and a ReLU non-linear activation function, making the network deep and highly non-linear. This significant expansion in dimensionality is crucial, as suggested by the original Barlow Twins work [34], to enable effective redundancy reduction during the self-supervised loss computation. The final output of the projector is then used in the loss calculation. For downstream tasks, we used the 128-dimensional output from the fusion MLP (before the projector) as the final pixel embedding. The TESSERA

encoder (up to the fusion MLP) has approximately 46 million parameters, while the projector accounts for the majority of the model’s  $\sim 1.4$  billion parameters.

**Table 2** Architectural parameters of the TESSERA v1.0 model.

Component	Parameters	Percentage of Total
<b>Encoder (Feature Extractor)</b>	<b>45,697,026</b>	<b>3.29%</b>
Sentinel-1 Encoder	22,846,465	1.64%
Sentinel-2 Encoder	22,850,561	1.64%
<b>Fusion MLP</b>	<b>131,200</b>	<b>&lt;0.01%</b>
<b>Projector (for Training only)</b>	<b>1,344,700,421</b>	<b>96.71%</b>
<b>Total Parameters</b>	<b>1,390,528,647</b>	<b>100.00%</b>

### *Self-Supervised Training*

The TESSERA model is trained using a modified Barlow Twins objective function [34]. For this objective, two distorted views, denoted as  $Y_A$  and  $Y_B$ , are generated for each input d-pixel. In TESSERA, these views are created by independently running the temporal sampling and preprocessing pipeline twice for the Sentinel-1 and Sentinel-2 data associated with a given d-pixel. This process involves:

1. For each view, independent sampling of a fixed number of valid observation dates from the annual Sentinel-2 time series (10 spectral bands).
2. For each view, independent sampling of a fixed number of valid observation dates from the annual Sentinel-1 time series (2 polarizations).

These views represent different, valid, but inherently incomplete glimpses of the pixel’s true temporal-spectral evolution, akin to observing the same location through intermittent cloud cover or from different satellite passes at different times. The model learns by reconciling these partial views. The inherent differences between the Sentinel-1 SAR and Sentinel-2 MSI modalities further provide diverse perspectives on the same underlying physical processes. Thus, our augmentations are fundamentally about sampling from the available, inherently incomplete information streams, rather than artificially distorting a complete input.

The network processes these two views ( $Y_A, Y_B$ ) through the dual-encoder and the projector to produce batch-normalized embeddings  $Z_A$  and  $Z_B$ . The standard Barlow Twins loss function,  $\mathcal{L}_{BT}$ , is defined as [34]:

$$\mathcal{L}_{BT} = \sum_i (1 - C_{ii})^2 + \lambda_{BT} \sum_i \sum_{j \neq i} C_{ij}^2 \quad (7)$$

Here,  $C$  is the cross-correlation matrix computed between the batch-normalized embeddings  $Z_A$  and  $Z_B$ . The indices  $i$  and  $j$  iterate over the dimensions of the embedding vectors. The first term (invariance term) encourages similar embeddings for different views of the same input ( $C_{ii} \rightarrow 1$ ). The second term (redundancy reduction term) promotes information efficiency by minimizing the correlation between different

embedding dimensions ( $C_{ij} \rightarrow 0$  for  $i \neq j$ ), weighted by  $\lambda_{BT}$ . We used the value of  $\lambda_{BT} = 5 \times 10^{-3}$  as recommended in Reference [34].

To further enhance the robustness of the model and mitigate overfitting, TESSERA incorporates an additional mix-up regularization term  $\mathcal{L}_{MIX}$ , inspired by Bandara et al. [108]. For each training batch, this involves shuffling one set of views (e.g.,  $Y_B$ ) along the batch dimension to create  $Y_S = \text{Shuffle}(Y_B)$ , then generating a mixed view  $Y_M = \alpha_{mix}Y_A + (1 - \alpha_{mix})Y_S$ . The mixing coefficient  $\alpha_{mix}$  is sampled from a uniform distribution on the unit interval,  $\alpha_{mix} \sim U(0, 1)$ . The embeddings  $Z_M$  and  $Z_S$  are obtained from their respective views. The mix-up loss penalizes deviations from the assumption that a linear interpolation in the input space corresponds to a linear interpolation in the embedding space.

$$C_{target}^{MA} = \alpha_{mix}(Z_A)^T Z_A + (1 - \alpha_{mix})(Z_S)^T Z_A \quad (8)$$

$$C_{target}^{MS} = \alpha_{mix}(Z_A)^T Z_S + (1 - \alpha_{mix})(Z_S)^T Z_S \quad (9)$$

$$\mathcal{L}_{MIX} = \frac{1}{2}(\|C^{MA} - C_{target}^{MA}\|_F^2 + \|C^{MS} - C_{target}^{MS}\|_F^2) \quad (10)$$

where  $C^{MA} = (Z_M)^T Z_A$  and  $C^{MS} = (Z_M)^T Z_S$  are the actual cross-correlation matrices from the model output. The total loss function optimized during training is a weighted sum:

$$\mathcal{L}_{total} = \mathcal{L}_{BT} + \lambda_{mix}\mathcal{L}_{MIX} \quad (11)$$

where  $\lambda_{mix}$  controls the strength of the mix-up regularization. We found  $\lambda_{mix} = 1.0$  (as recommended by [108]) to be effective based on our experiments.

The TESSERA model was pre-trained using approximately 800 million d-pixels drawn from 3,012 globally distributed Military Grid Reference System (MGRS) tiles chosen from the years 2017-2024. d-pixels were generated by spatially downsampling Sentinel-1 and Sentinel-2 data by a factor of 400. This was achieved by systematically taking every 20th pixel along the horizontal and vertical axes. Each d-pixel contained the annual time series for 10 spectral bands of Sentinel-2 data and the annual time series of VV and VH polarizations for Sentinel-1 data.

For each pixel location, after removing invalid observations (e.g., due to cloud cover for Sentinel-2), we performed sparse temporal sampling. This involves randomly selecting a fixed number of 40 valid observation dates from the year's data. The sequence length for the Transformer encoders was fixed at 40 timesteps for both modalities. If there are fewer than 40 cloud-free dates, replacement sampling is performed. This strategy standardizes the input sequence length and serves as a key data augmentation mechanism, building invariance to data gaps and teaching the model that the underlying signal persists regardless of the specific dates observed. Finally, these values were standardized using global statistics to stabilize training. The temporal context of each sampled observation was encoded by transforming its normalized Day-of-Year (DOY) into sine and cosine features, which were then concatenated with the corresponding spectral or backscatter measurements.

As we were in a compute-limited rather than data-limited pre-training regime, we trained for a single epoch, which corresponded to approximately 6200 GPU hours on 16 AMD MI300X GPUs (192GB memory each). We used PyTorch with Fully Sharded

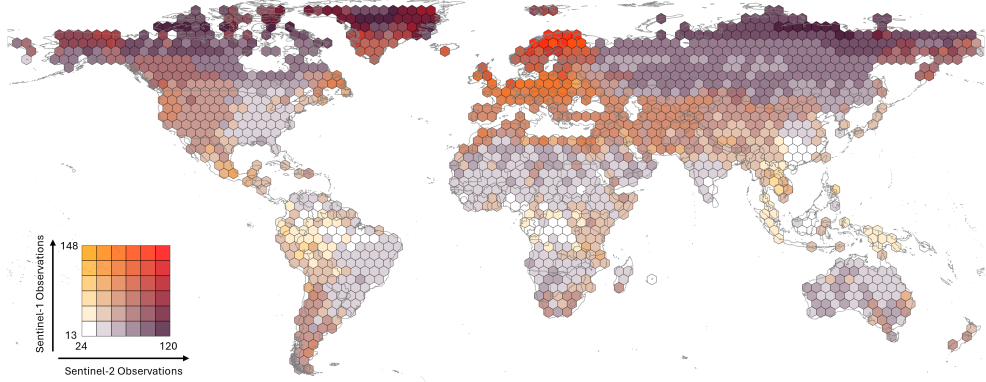


**Fig. 8 TESSERA is trained on globally-distributed training data.** TESSERA was trained on over 3000 MGRS tiles distributed globally from 2017 to 2024. The colour of each hexagon in the map corresponds to the average number of valid observation days for Sentinel-1 (S1) and Sentinel-2 (S2), as defined by the bivariate colour legend. This visualization highlights the density of combined S1 and S2 observations available for training across different regions, ensuring the model learns from a diverse range of geographical and environmental conditions.

Data Parallel (FSDP) and Automatic Mixed Precision (AMP) enabled. AdamW optimizer was used with a base learning rate of 0.002 and weight decay of  $1 \times 10^{-6}$ . The learning rate schedule consisted of a linear warmup during the initial 10% of steps, followed immediately by a cosine decay for the remainder of training. The global batch size was 32,768. Key training dynamics, including loss curves, learning rate schedule, and evolution of downstream performance during pre-training, are visualized in Supplementary fig. 9.

A crucial aspect of our training methodology is a data shuffling strategy, essential for learning globally representative features from a representative sample of a vast and geographically diverse dataset. Given that d-pixels within an individual MGRS tile exhibit high spatial autocorrelation, a naive sequential or locally-shuffled data loading process would expose the model to strong geographic biases in each batch. To overcome this, we developed a custom data processing pipeline to implement a truly global shuffle across all  $\approx 800$  million training samples, which constituted more than 2 TB of initial d-pixel data. This pipeline is conceptually illustrated in Fig. 10a.

The impact of this approach on training stability is empirically demonstrated in Fig. 10b. Compared to a conventional localized shuffling strategy, which results in a highly volatile loss curve (top plot), our global shuffling strategy yields a markedly smoother and more stable convergence (bottom plot). This enhanced stability is fundamental for robust convergence and for preventing the model from overfitting to regional characteristics.

Operationally, the process begins with the aggregation of d-pixels from all MGRS tiles into a single, comprehensive pool. A global shuffling operation is performed on this pool, a critical step to break the spatial contiguity of data from individual tiles and ensure each training batch contains a diverse mix of geographical and environmental contexts. Following this global shuffle, the data augmentation required by the Barlow

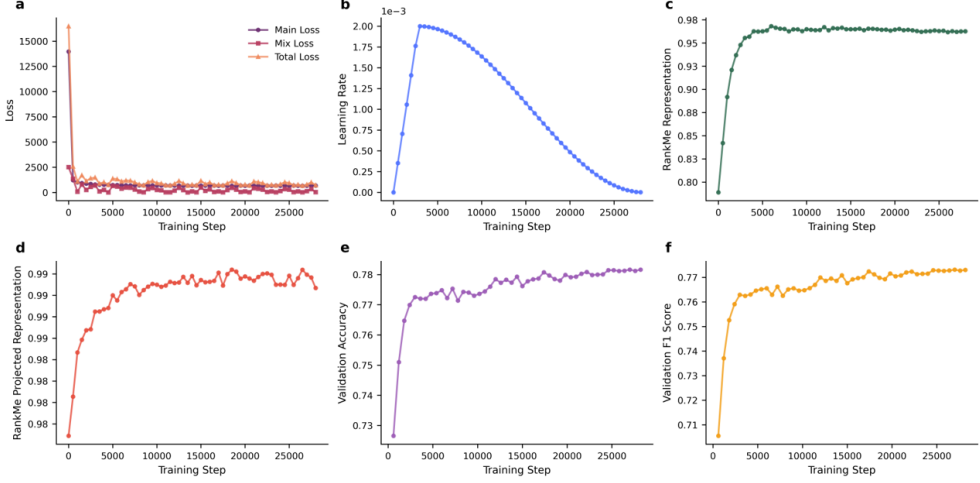


**Fig. 9** Training dynamics curves show that TESSERA rapidly reaches its asymptotes. **a**, Training loss curves, showing the main Barlow Twins loss, the mixup regularization loss, and the total loss. **b**, The learning rate schedule, consisting of a linear warmup phase followed by a cosine decay. **c**, RankMe score calculated on the high-dimensional (16,384-D) output of the projector, which quickly saturates, indicating the model is effectively utilizing the large feature space for redundancy reduction. **d**, RankMe score of the final 128-D fused representation, showing that the embeddings used for downstream tasks become progressively richer and less redundant. **e**, **f**, Downstream performance on the Austrian crop classification validation set, tracked by accuracy and F1 score respectively during pre-training, showing a steady improvement that correlates with the training progress.

Twins framework is applied. As detailed in the Supplementary Text, this involves generating two distinct augmented views (e.g.,  $Y^A$  and  $Y^B$ ) for each d-pixel.

To manage the significant I/O demands of shuffling and augmenting such a large volume of data, we developed a custom high-performance pipeline that handles the reading of raw d-pixel data, executes the global shuffle, and prepares the data for augmentation. The resulting pairs of augmented d-pixels are then serialized into a compact, pickle-like file format. These files are organized into manageable chunks and loaded by PyTorch *DataLoader* workers, which stream the data and assemble the final training batches. This end-to-end pipeline ensures that each batch presented to the model is a well-shuffled, globally diverse representation of Earth’s surface characteristics, which is fundamental for training a robust pixel-wise foundation model like TESSERA.

#### Global Embedding Map Generation

A primary output of the TESSERA project is the generation of annual global embedding maps with 10 meter resolution for the years 2017-2024. To generate these maps, the pre-trained and frozen TESSERA dual encoder (excluding the projector) is used. For each 10 meter pixel on the globe and for each year:

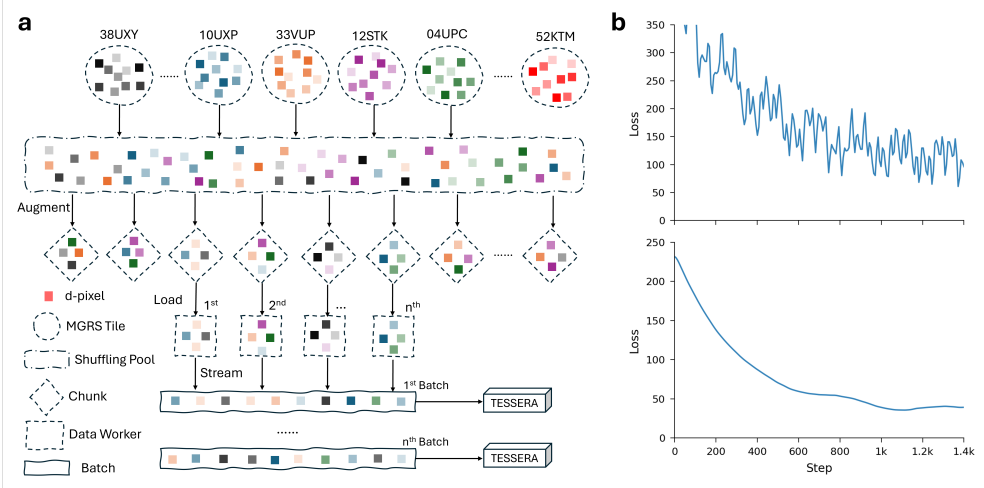


**Fig. 10 Data shuffling greatly improves training stability.** **a**, Schematic of the data shuffling and loading process. D-pixels (coloured squares) from thousands of MGRS tiles are first aggregated into a global pool. A custom Rust binary [37] performs a global shuffle on this multi-terabyte dataset before applying augmentations. The processed data is then organized into chunks and streamed by data workers to form well-shuffled, globally diverse training batches. **b**, Comparison of training loss curves. The top plot shows the volatile loss progression typical of a localized shuffling strategy, which is susceptible to geographic bias. The bottom plot shows the significantly smoother and more stable loss curve achieved with our global shuffling pipeline, demonstrating more effective and robust model convergence.

1. The full Sentinel-1 and Sentinel-2 time series data at 10 meter resolution are acquired and pre-processed to form d-pixels. Unlike pre-training, no spatial downsampling is performed at this stage.
2. A fixed number of 40 timesteps is sampled from the valid observations within the year for both Sentinel-1 and Sentinel-2 data, along with their DOY positional encodings.
3. These sampled time series are fed into their respective frozen TESSERA encoders.
4. The outputs from the S1 and S2 encoders are fused by the MLP, producing a 128-dimensional embedding vector for that pixel for that year.

This process is repeated for all land pixels globally to create an annual embeddings map of shape (H, W, 128), where H and W are the dimensions of the global 10 meter grid.

## A.2 Scaling with data and network size

To identify an optimal and efficient architecture for TESSERA, and to understand the scaling properties of our model, we conducted a series of experiments using the Austrian crop classification task as the downstream task. Our investigation focused on two main areas: the impact of the projector network's dimensions and the overall model scaling laws concerning performance versus computational cost (Fig. 11).

Our experiments revealed that the performance of the final embeddings on the chosen downstream task of crop classification in Austria was relatively insensitive to the size of the Transformer encoders. We found that using 4 transformer layers, each with 4 attention heads, provided a strong baseline without incurring excessive computational overhead during inference. This makes the feature-extracting part of the model computationally efficient.

In contrast, the architecture of the projector network proved to be critical for effective self-supervised learning. As detailed in Section A.1, the full projector is a six-layer MLP, consisting of an input and an output layer for accommodating dimensional changes, and four core hidden layers. Our parameter sweep focused on this computationally intensive hidden block. We varied the number of these hidden layers (referred to as 'depth' in Fig. 11a) and their width (number of neurons per layer), with results shown in Fig. 11a. As discussed by Zbontar et al. [34], deeper and wider projectors consistently improved performance, as measured by the validation F1 score in the downstream task. The highest validation score was achieved with the largest configuration tested (8 hidden layers, 32,768 neurons wide). However, this configuration led to an out-of-memory error with our standard global batch size; therefore, we halved the batch size to 16,384 to enable stable training for this specific setup, indicated by the dagger symbol ( $\dagger$ ) in the figure. For the final TESSERA v1.0 model, we selected the configuration with four hidden layers and a width of 16,384, marked with a star (\*), as it provided a strong balance between high performance and computational efficiency. Furthermore, we analysed the relationship between model performance,

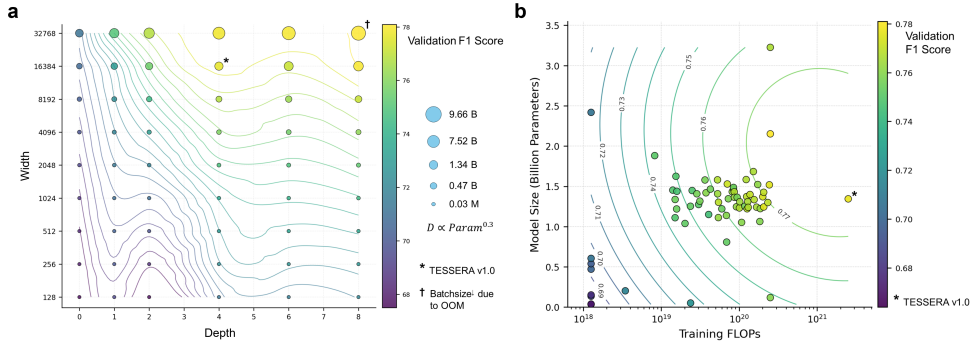


**Fig. 11 Model performance improves with increasing projector size and additional computation.** **a**, Hyperparameter sweep for the projector network's architecture. Each point represents a configuration, with its position determined by the number of hidden layers (depth, x-axis) and their width (y-axis). The colour and size of the point indicate the validation F1 score and the number of parameters, respectively. Performance generally increases with both width and depth. The dagger ( $\dagger$ ) marks the configuration with the highest F1 score, which required a reduced batch size due to memory constraints. The star (\*) indicates the final configuration selected for TESSERA v1.0, representing a balance between performance and efficiency. **b**, Scaling laws for TESSERA. The plot shows the validation F1 score as a function of training FLOPs and model size (in billions of parameters). A clear positive correlation is visible, indicating that performance improves as more computational resources and larger models are used. The final TESSERA v1.0 model is marked with a star (\*) to demonstrate its position within this scaling trend.

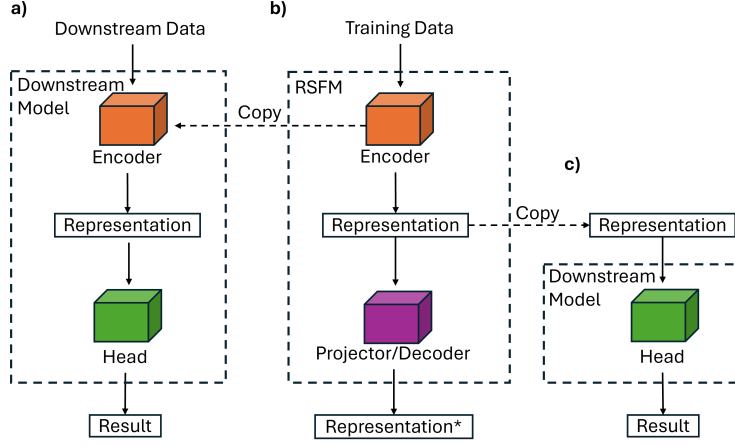


**Fig. 12 Unlike common Remote Sensing Foundation Models (RSFM), TESSERA simplifies downstream task applications.** Most existing RSFMs use approach (a) where, after training, the encoder is extracted and combined with a task-specific head to form a new model for downstream tasks. Users can then fine-tune the entire model or only the head. Another approach (b) is where both the encoder and the projector (or decoder) are typically updated. In contrast, the TESSERA approach (c) uses pre-generated embeddings directly as input. This results in lightweight downstream models that consist only of a task-specific head.

the number of trainable parameters, and the total training computation (FLOPs), as shown in Fig. 11b. The results demonstrate a clear scaling trend: model performance improves predictably with increases in model size and computational budget. This confirms that TESSERA’s performance can be further enhanced with greater computational resources, following established scaling laws for large neural networks. The final TESSERA v1.0 model is marked with a star (\*) on this curve, highlighting its position as a model that balances state-of-the-art performance with cost-effective training requirements.

### Ablation study

**Table 3 The ablation study demonstrates that data shuffling and mixup regularization are essential, Sentinel 1 data adds little additional value, and that quantization has nearly no impact on performance.** We study downstream crop classification performance on the 100x-downsampled Austrian crop dataset. The baseline represents the full model. Each subsequent row shows the result of removing the specified component. Performance is measured by validation F1 score and the RankMe score. Arrows ( $\uparrow$ ) indicate that higher values are better. The results demonstrate that all components contribute positively to the model’s overall performance.

Configuration	Validation F1 Score ( $\uparrow$ )	RankMe Score ( $\uparrow$ )
Baseline (Full Model)	0.773	0.963
w/o Global Data Shuffling	0.681	0.847
w/o Mixup Regularization	0.662	0.857
w/o Sentinel-1 Data	0.742	0.931
w/o Shuffling & Mixup	0.626	0.867
w/o Embedding Quantization	0.779	0.972

To validate the contribution of each key component within the TESSERA framework, we performed an ablation study. We systematically removed or disabled individual components from our full model (the baseline) and evaluated the impact on the 100x downsampled Austrian crop classification dataset.

Performance was evaluated using two metrics: the standard validation overall F1 score, and a measure of the effective rank of the learned embeddings, which we refer to as the RankMe score [109]. The RankMe score quantifies the richness of the embeddings by measuring how uniformly the information is distributed across the feature dimensions. Given a batch of embeddings represented by the matrix  $Z \in \mathbb{R}^{N \times D}$ , where  $N$  is the batch size and  $D$  is the embedding dimension, we first compute its singular values  $s_1, s_2, \dots, s_D$ . These are normalized to form a probability distribution  $p_i = s_i / \sum_j s_j$ . The RankMe score is the Shannon entropy of this distribution, normalized by the maximum possible entropy:

$$\mathcal{R}_{\text{RankMe}} = \frac{-\sum_{i=1}^D p_i \log(p_i)}{\log(D)} \quad (12)$$

A score closer to 1 indicates that the embeddings are of higher effective rank, utilizing the full dimensionality of the feature space more effectively to create richer, less redundant representations.

The results of the ablation study are summarized in Table 3. Our analysis reveals several key insights into the model’s architecture and training strategy. The most critical component turns out to be the global data shuffling pipeline, which is designed to break spatial autocorrelation and present the model with geographically diverse mini-batches. Removing mixup regularization also severely degrades results. When both are removed, the model’s performance collapses, showing that the combination of global shuffling and mixup regularization is needed to prevent overfitting and to learn generalizable robust representations.

With removal of Sentinel-1 data, task performance decreases moderately, demonstrating some gain from the fusion of optical and SAR data yields. However, performance is still relatively good even with only Sentinel-2 data. This highlights both TESSERA’s overall robustness and its continued efficacy in regions or historical periods where Sentinel-1 data are sparse or unavailable, which is not uncommon in practice.

Finally, the effect of quantization is particularly noteworthy. We employ Quantization-Aware Training (QAT) to convert the embeddings from 32-bit floating-point (float32) to 8-bit integer (int8) format. Removing this quantization step (i.e. using full float32 precision) results in a marginal performance improvement. This demonstrates the success of our QAT strategy: we achieve a nearly four-fold reduction in the storage and bandwidth requirements for our final data products, with a negligible impact on embedding quality. This underlies our “Embeddings-as-Data” approach, making global-scale high-resolution analysis practical: Without this, each year’s embeddings would consume 1PB, making the hosting of 8 years of embedding costly and likely unachievable.

### A.3 Downstream Task Application Methodology

A core motivation for self-supervised learning with foundation models is the creation of task-agnostic feature embeddings that can be effectively transferred to various downstream tasks, particularly in scenarios with limited labelled data. Having pre-trained TESSERA on large unlabelled datasets, we evaluated the utility of its learned embeddings across different remote sensing applications. The evaluation methodology involves using pre-trained TESSERA encoders as fixed feature extractors.

The pipeline for applying TESSERA embeddings to downstream tasks is as follows (illustrated in the Supplementary fig. 12):

1. **Download Embeddings for the Region of Interest:** The GEOTESSERA Python library [37] allows users to download embeddings for a desired region and year in the form of a numpy array.
2. **Prepare labelled Downstream Data:** The labelled dataset for the target task (e.g., pixel-level crop-type labels, canopy height measurements, or land use change polygons) is prepared.
3. **Design Task-Specific Head:** A lightweight, task-specific neural network module (the "head") is designed. This head takes the extracted TESSERA embeddings as input.
  - For pixel-wise classification (e.g., crop classification), the head is typically a shallow MLP (1-3 layers) ending in a softmax output layer.
  - For pixel-wise regression (e.g., canopy height regression), the head is usually an MLP ending in a single linear output neuron.
  - For tasks requiring spatial context from the embeddings (e.g., canopy height mapping over an area, semantic segmentation), the input to the head can be a patch of TESSERA embeddings (e.g.,  $64 \times 64 \times 128$ ). The head might then be a convolutional architecture, such as a UNet, that processes these spatial feature maps to produce dense predictions.
4. **Train Downstream Head:** Only the parameters of this newly defined task head are trained using the extracted TESSERA embeddings as input features and the corresponding labels. Standard supervised learning techniques, optimizers (e.g., Adam), and task-appropriate loss functions (e.g., Cross-Entropy for classification, Mean Squared Error for regression) are used. This training typically requires significantly less labelled data and computational power compared to training a deep model from scratch.
5. **Evaluation:** Once the head is trained, inference is performed on a test set by extracting TESSERA embeddings for the test samples and passing them through the trained head. Performance is evaluated using standard metrics relevant to the task.

This workflow allows the use of TESSERA embeddings in a range of diverse applications, demonstrating its role as a foundational model for geospatial analysis.

TESSERA users who would like to generate their own embeddings can load the frozen weights from the saved pre-training checkpoint into the TESSERA dual encoder architecture. For each input sample (e.g., pixel, object, or patch) in the region of

interest, its corresponding Sentinel-1 and Sentinel-2 time series data for the relevant year must be downloaded and processed using the d-pixel creation pipeline. These d-pixels are passed through the frozen encoders and their outputs are fused by the MLP to generate the final 128-dimensional TESSERA embedding for that sample. To enhance stability, multiple embeddings can be created with different random temporal samples and averaged.

#### A.4 Downstream Task: Austrian Crop Classification

##### *Dataset and Preprocessing*

We used the publicly available INVEKOS dataset for Austria, focusing on the 2022 growing season [44]. The data set originally contained 154 crop types, which we grouped into 17 broader classes (for example, combining sugar beet and feed beet) based on phenological similarity and sample availability to ensure robust training and evaluation. For each pixel in the dataset, we extracted its corresponding 128-dimensional TESSERA embedding from our generated 2022 global embeddings map.

##### *Pixel-wise Classification Baselines*

To provide a comprehensive performance comparison, we implemented three distinct models for pixel-wise classification:

- **TESSERA + MLP:** The primary model, where the frozen 128-dimensional TESSERA embeddings were used as input to a simple MLP. The MLP consisted of two hidden layers with 256 and 128 neurons, respectively, using ReLU activation functions, followed by a softmax output layer for the 17 classes.
- **PRESTO + MLP:** For a direct and fair comparison with a leading foundation model, we used the official pre-trained PRESTO model [19] to generate its pixel embeddings. These embeddings were then fed into an MLP head identical to the one used for TESSERA.
- **GSE + MLP:** To include another key foundation model, we used the publicly available Google AphaEarth Satellite Embedding (GSE) V1 dataset [39]. These embeddings were similarly fed into an MLP head identical to the one used for TESSERA.
- **Random Forest:** As a traditional baseline, we trained a Random Forest (RF) classifier directly on raw time-series data. For each pixel, we utilized all available Sentinel-1 (2 polarizations) and Sentinel-2 (10 spectral bands) observations throughout the year. The temporal and spectral/polarization dimensions were flattened and concatenated to form a single 1256-dimensional feature vector. The RF model was configured with 100 trees, while all other hyperparameters retained their default values as implemented in the SCIKIT-LEARN library.

For the experiments shown in the main text’s figure, we trained these models on randomly selected subsets of the data (from 1% to 30% for panel a; specified samples-per-class for panel b), using a fixed validation set for hyperparameter tuning and a held-out test set for final evaluation.

**Table 4** Pre-training hyperparameters for the **TESSERA** v1.0 model.

Description	Symbol	Value
<b>Optimizer &amp; Schedule</b>		
Optimizer	-	AdamW
Batch Size (Per-GPU)	$B_{local}$	2,048
Batch Size (Global)	$B_{global}$	32,768 (16 GPUs $\times$ 2,048)
Epochs	-	1
Base Learning Rate	$\eta$	0.002
Weight Decay	$\lambda_{wd}$	$1 \times 10^{-6}$
Learning Rate Schedule	-	Linear warmup (10%) followed by cosine decay
Gradient Clipping Norm	-	2.0
<b>Loss Function</b>		
Barlow Twins Lambda	$\lambda_{BT}$	$5 \times 10^{-3}$
Mixup Lambda	$\lambda_{mix}$	1.0
<b>Architecture &amp; Data</b>		
Sequence Length	$L$	40
Representation Dimension	$D_{repr}$	128
Projector Output Dimension	$D_{proj}$	16,384
Quantization Bits (QAT)	-	8

### *Patch-wise Semantic Segmentation*

To assess spatial-contextual performance, we conducted a semantic segmentation experiment. The approach varied based on the foundation model’s architecture:

- For the foundation models capable of generating pixel-wise embeddings, namely **TESSERA**, **PRESTO** [19], and **GSE** [39], a distinct workflow was used. We first construct patches from their pixel-level embeddings (e.g., a data cube of size  $H \times W \times C$ ). These patches were then fed into a standard **UNet** architecture [76], which learns to model the spatial relationships between the embeddings to produce a segmentation map. It is noteworthy that while TESSERA and PRESTO’s base embeddings do not explicitly model spatial context, GSE’s do. However, their shared ability to generate pixel-level outputs makes them suitable for this UNet-based downstream approach.
- For other foundation models that are inherently patch-based (e.g., Prithvi [110], Sat-las [15]), their encoders already process image patches. Therefore, for these models, we only attach and train a **UPerNet decoder head** to their encoders to generate the final segmentation output. We did not freeze the encoders during the fine-tuning.

Performance was measured using mean Intersection over Union (mIoU) and macro F1 scores. A visual comparison for example patches is provided in Supplementary Fig. 13.

### *Embedding Space Analysis*

The 2D visualizations shown in the main text (Figure 3 d) were generated by applying the Uniform Manifold Approximation and Projection (UMAP) [45] algorithm to the embeddings of every pixel within the Austrian study area. UMAP is a non-linear dimensionality reduction technique based on Riemannian geometry and algebraic topology. It constructs a weighted k-nearest neighbour graph in the original high-dimensional space, then optimizes a low-dimensional projection to primarily preserve

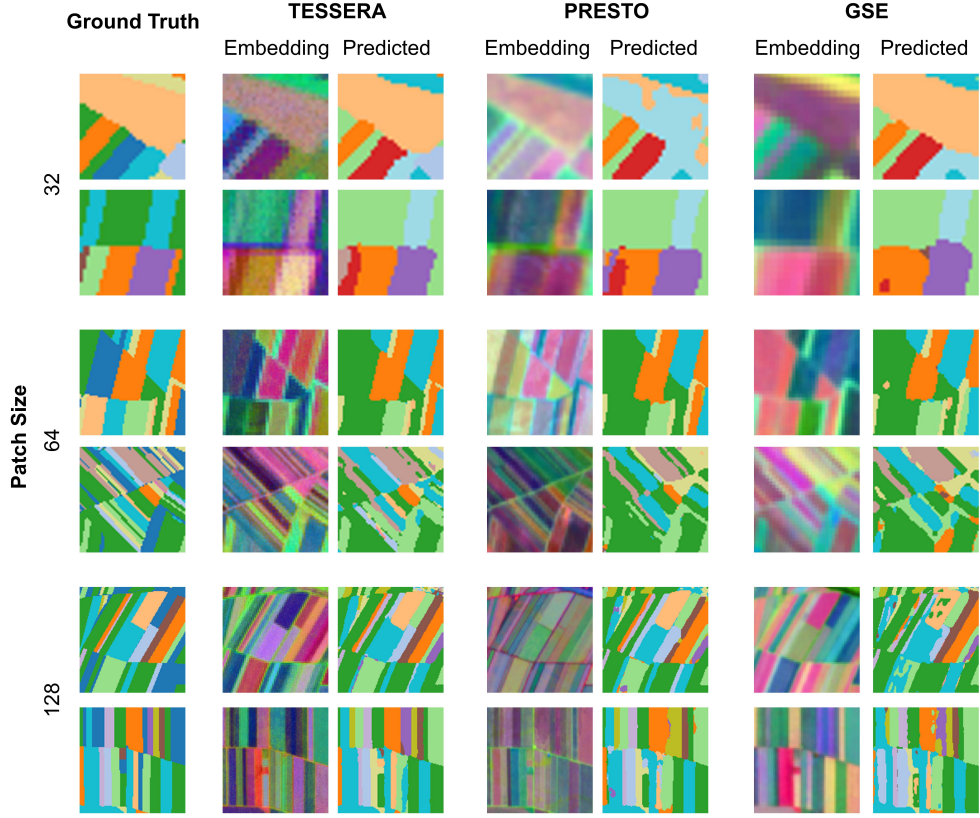


**Fig. 13 TESSERA predictions most closely resemble the ground truth for patch-based semantic segmentation.** Each row corresponds to a different patch size (32x32, 64x64, 128x128). The first column shows the ground truth segmentation. For each model (TESSERA, Presto, and GSE), two columns are displayed: a PCA visualization of the input embeddings for the patch (labelled 'Embedding') and the final predicted segmentation map (labelled 'Predicted').

local distances and local structure. UMAP, like other non-linear techniques such as t-SNE and LargeVis, is designed to preserve local relationships within high-dimensional data; however, it is also able to retain more of the global structure, making it particularly effective for understanding both fine-scale and broader patterns in the embedding space. In this work, the entire embedding map (for example, a shape array  $H \times W \times 128$ , where  $H$  and  $W$  are the height and width of the region) was used as a direct input to UMAP for the TESSERA, PRESTO, and GSE embeddings.

To quantitatively measure the quality of the clustering in the original 128-dimensional space, we calculated the Silhouette score and the Davies-Bouldin Index.

- The **Silhouette score**,  $s(i)$ , for a single data point  $i$  measures how similar it is to its own cluster compared to other clusters. It is defined as:

$$s(i) = \frac{b(i) - a(i)}{\max(a(i), b(i))} \quad (13)$$

where  $a(i)$  is the mean distance between  $i$  and all other points in the same cluster, and  $b(i)$  is the mean distance from  $i$  to all points in the nearest neighbouring cluster. The score ranges from -1 to 1, where a high value indicates that the object is well matched to its own cluster and poorly matched to neighboring clusters.

- The **Davies-Bouldin Index** (DBI) evaluates clustering quality by computing the ratio of within-cluster scatter to between-cluster separation. For a set of  $k$  clusters, it is defined as:

$$\text{DBI} = \frac{1}{k} \sum_{i=1}^k \max_{j \neq i} \left( \frac{\sigma_i + \sigma_j}{d(c_i, c_j)} \right) \quad (14)$$

where  $\sigma_i$  is the average distance of all points in cluster  $i$  to their centroid  $c_i$ , and  $d(c_i, c_j)$  is the distance between the centroids of clusters  $i$  and  $j$ . Lower DBI values indicate better clustering, with a score of 0 representing the ideal case where the clusters are compact and well separated.

## A.5 Downstream Task: Canopy height estimation

### *Study Areas and Ground Truth Datasets*

Canopy height prediction was evaluated in a  $5 \times 6$  km area in the Danum Valley, Borneo. This region is covered in tropical rainforest dominated by species in the Diptocarpaceae family, which hosts some of the tallest trees in the tropics [111, 112]. Ground truth data was derived from airborne laser scanning (ALS) performed in February 2020 [66]. ALS data provides detailed 3D point clouds of vegetation and terrain structure, which were processed using the LSPIKEFREE algorithm [113] to estimate top-of-canopy height at 1 m resolution. These canopy height rasters were then downsampled using mean pooling to 10 m to match the resolution of the TESSERA representations.

### *Modelling methods*

To predict the canopy height from the different embeddings, we used a standard U-Net architecture [76]. It takes as input a  $32 \times 32$  pixel patch (covering a  $320 \times 320$  m area) of representations. For 128-dimensional embeddings (as in TESSERA and PRESTO), this results in a  $32 \times 32 \times 128$  data cube. The network outputs a single-band  $32 \times 32$  raster of predicted canopy height values. The proposed U-Net contains approximately 30 million parameters and was trained for 200 epochs using a batch size of four patches. At the end of each epoch, the model was evaluated using validation data and the model with the best performance on the validation set was retained for the final evaluation. In practice, training usually converged within the first 20 epochs, with rare boosts in performance later in training. Model training was done in Python using PyTorch.

To ensure spatial generalization and avoid overfitting local patterns, the reference data were divided into training, validation, and test sets that are spatially disjoint. Each study region was divided into four spatial folds based on cardinal directions (bottom, top, left, right), each fold covering 50% of the area. For each fold, the remaining half of the region was used for training and validation. To account for inherent model randomness, we trained three independent models per fold, resulting in 12 trained models for each foundation model. This strategy captures variability due to both spatial heterogeneity and training randomness. The final performance of the model was evaluated on the test data held using the following metrics: coefficient of determination ( $R^2$ ), root mean square error (RMSE), and mean bias.

### ***Baselines***

TESSERA, PRESTO [19], and GSE [39] embeddings were compared by training identical models using each representation as input, with all other settings held constant. Each model was trained for 200 epochs on the same data split, and the version achieving the best validation performance was selected for final evaluation on the held-out test set.

To benchmark performance against classical remote sensing approaches applied at the global scale, we compared the predictions against three global canopy height products: Potapov et al. [2021][59] (GLAD), Lang et al. [2023][58] (ETH), and Tolan et al. [2024][60] (Meta) as well as a regional map produced by Lang et al. [2021][68]. These maps were downloaded at 10 m resolution from Google Earth Engine and compared directly to the canopy height derived from ALS. Although there are some temporal mismatches between ALS acquisition (2020) and global products, we assume relative stability of canopy height in the short term in this region, which is reasonable given that the area was not logged or burned.

Finally, we trained the U-Net model using Sentinel-2 input as a baseline. This approach retained the same model architecture, patch size, and evaluation setup, but replaced embeddings with cloud-free annual median composites of Sentinel-2 imagery. Cloud masking and compositing were performed in GEE, resulting in 12 channel input images, with one channel for each Sentinel-2 spectral band. Although different Sentinel-2 bands have different spatial resolutions, all were resampled to 10 m to match the FM pipelines.

## **A.6 Downstream Task: Burned area detection**

### ***Study Areas and Ground Truth Datasets***

For fire disturbance detection, two  $15 \times 15$  km tiles in California were selected at random from the training sample pool in the burn scars benchmark dataset [114], referred to as Burn Area A and Burn Area B. Each Burn Area contains over two million 1 m pixels. Burn Area A is a heterogeneous landscape of forests, shrublands, agricultural land, and built infrastructure. In 2020, it experienced two separate wildfires: the 'Quail Fire' in June ( $\sim 730$  ha) and the much larger 'Hennessey Fire' in August ( $\sim 121,000$  ha). Burn Area B experienced a single large fire ('Glass') ( $\sim 27,500$  ha) in September 2020 that mainly affected forested land. In all cases, most of the impact of the fire occurred in vegetated areas composed of forest and shrubland. To classify

the dominant land cover types in the burn areas, we used the Dynamic World Land Cover data set [115].

The dataset from the Monitoring Trends in Burn Severity (MTBS) program [95] was used to identify burned areas and severity of the burn. Fire ignition and containment dates, as well as fire perimeters, were obtained from the MTBS burned area boundaries dataset. Burn severity, defined as the measure of ecological damage caused by fire [116], was derived from categorical and continuous severity metrics provided by MTBS. To obtain burn severity categories of low, medium, and high, as well as continuous burn severity, we used the annualized MTBS burn severity dataset as well as individual severity maps for each fire. MTBS calculates severity using two primary indices: the differenced NBR (dNBR) and its relativized form (RdNBR), both calculated from pre- and post-fire Landsat images. Low severity typically indicates limited ecological impact, while high severity reflects significant ecological disruption and vegetation mortality [116]. Since MTBS datasets are derived from Landsat, they are provided with a resolution of 30 m and were upsampled to 10 m to match the resolution of the TESSERA representations. The MTBS and Dynamic World datasets were downloaded as 10 m rasters from Google Earth Engine [102]. For our classification analysis, we define “unburned” pixels using MTBS class 0 and “burned” pixels as MTBS classes 2 (low), 3 (moderate) and 4 (high). The ambiguous “unburned/low” class (1) was excluded to ensure a clear binary classification benchmark.

### ***Dimensionality Reduction***

We used UMAP (Uniform Manifold Approximation and Projection) [45] to reduce 128 dimensions of TESSERA embeddings to 2D for visual inspection of FM representations in areas affected by wildfires. We applied the dimensionality reduction to 128-dimensional TESSERA embeddings and visualized the resulting 2D projections. To interpret the structure of the projected clusters, we colour coded points according to different annotation schemes: burn state (burned vs. unburned), land cover class, or burn severity. These visualizations helped us assess whether FM embeddings spatially separate ecological conditions of interest. To reduce computational cost and improve legibility, we randomly subsampled a subset of pixels prior to applying the dimensionality reduction. UMAP projections were additionally used to classify pixels into unburned, low, moderate, and high-severity classes using a random forest (RF) classifier, to quantify the separability in the UMAP embedding space. UMAP projections were computed using the UMAP-LEARN Python library and RF was implemented using the SCIKIT-LEARN Python library.

### ***Label Efficiency Analysis and Baselines***

We conducted a label efficiency experiment to evaluate the performance of a random forest classifier when only a limited amount of labelled data is available. The valid pixels from both study areas were combined and split into a fixed test set (20%) and a training set. We then trained multiple classifiers on progressively smaller stratified random subsamples of the full training set, with ratios ranging from 1.0 to 0.001%. The classifier used 100 estimators, a maximum depth of 12, minimum leaf samples of 20, and class\_weight=‘balanced’ to account for class imbalance. Performance was

measured using the macro-averaged F1 score between burned and unburned classes on the fixed test set.

We compared three types of input embeddings for the classification task. The first was TESSERA, using embeddings for 2020. The second was a task-specific composite baseline, constructed using prior knowledge of the fire event. This baseline consisted of median composites of 12 Sentinel-2 bands, with the Normalized Burn Ratio (NBR), and Normalized Difference Vegetation Index (NDVI) calculated separately for a pre-fire window (October 2019–April 2020) and a post-fire window (October 2020–April 2021), then concatenated into a single feature vector. The third type of input was Google AlphaEarth Satellite Embeddings (GSE), using publicly available annual embeddings from the GSE V1 dataset [39]. GSE and task-specific composite images were downloaded as rasters from Google Earth Engine.

## A.7 Downstream Task: Above-ground biomass estimation

### *Dataset*

For the AGB regression task, we used the ground truth data from the BioMassters dataset [72]. This dataset covers nearly 11,500 forest patches in Finland, with each patch representing a  $2,560 \times 2,560$  m area at 10 meter pixel resolution. Above-Ground Biomass (AGB) values were determined using open forest airborne LiDAR data and an extensive network of field plots as reference measurements by the Finnish Forest Centre. Patch coordinates and collection years—provided by the authors of Ref. [72] upon request—were used to retrieve satellite imagery to generate TESSERA and Google AlphaEarth Satellite Embeddings (GSE) [39].

### *UNet model architecture*

To obtain AGB estimates, we trained a convolutional neural network based on the UNet architecture [76], using TESSERA or GSE embeddings [39] as input. The model received  $256 \times 256 \times 128$  and  $256 \times 256 \times 64$  input patches for TESSERA and GSE, respectively, where the dimension denotes the number of channels.

The network followed a standard UNet structure with two encoder and decoder stages. The encoder comprised two convolutional blocks with 256 and 512 channels, each consisting of two  $3 \times 3$  convolutions followed by batch normalization, ReLU activation, and  $2 \times 2$  max pooling. A 1024-channel bottleneck block was used prior to upsampling. The decoder mirrored the encoder, using transposed convolutions for upsampling and skip connections from the encoder, followed by double-convolution blocks. A final  $1 \times 1$  convolution produced the single-channel regression output. The model had approximately 30 million trainable parameters. The loss function was defined as the root mean squared error (RMSE) averaged over individual patches.

Following the evaluation protocol in Ref. [72], RMSE was computed on a test set of 2773 patches and reported as the average RMSE per patch. For limited label testing, a subset of labels was randomly chosen from the remaining data and randomly divided into training and validation sets (80:20). The UNet model was trained on the embeddings for 80 epochs, with the model achieving the lowest loss on the validation set selected as the final model. Figure 5 shows the average RMSE calculated over five random splits, with bars indicating the minimum–maximum range when it exceeds

the size of the dot. Training was performed with Adam Optimizer (learning rate = 1e-4, batch size = 4). Task-specific training on the entire dataset (80% training / 20% validation) using a single NVIDIA H200 GPU and 8 CPU cores took approximately 5 hours for TESSERA embeddings and 4 hours for the GSE embeddings.

### ***Baselines***

In addition to GSE, we compared the performance of TESSERA to two other baselines: the winner of the BioMassters competition [72] and the SpectralGPT foundation model [18] combined with a UPerNet [78].

For SpectralGPT, we used the implementation provided in Ref. [79], with the BioMassters satellite data as input, a lightweight spatial-temporal encoder L-TAE [77] for temporal aggregation, and a UPerNet as the regression head. This setup was found in [79] to outperform other tested foundation models on the BioMassters dataset. To ensure consistency in the limited label setting, we replaced the default sampling strategy with the same random splits used to evaluate TESSERA and normalized the inputs with their mean and standard deviation. Although we initially experimented with using per patch RMSE as the loss function to align with our evaluation metric, we ultimately reverted to the MSE loss [79] because it resulted in slightly better performance. Obtaining the results for the full dataset using a single NVIDIA H200 GPU took approximately 18 hours.

For evaluating the supervised baseline, we downloaded the pre-trained weights of the BioMassters winning model and ran inference on the test set, applying a post-processing step to clip predictions to a non-negative range. Although we attempted to retrain the model from scratch using two H200 GPUs and a different CUDA version than in the original setup, this configuration led to inferior performance compared to the original pre-trained model. According to the BioMassters codebase, the original model was trained on two A100 40GB GPUs over the course of eight days, highlighting the greater time efficiency of TESSERA, which required only five hours.

## **A.8 Downstream Task: Stocking indices in Voluntary Carbon Markets**

### ***Relative height modelling***

Participants in the voluntary carbon market can use a remotely sensed “stocking index” to quantify project additionality, that is, the degree to which the carbon sequestration in the project exceeds what would have occurred in the natural course of events. The chosen stocking index must be correlated with the above-ground biomass (AGB) of the observed objects, and the strength of the correlation must be demonstrated using a suitable in situ reference dataset.

To demonstrate the superior quality of the TESSERA embeddings compared to existing state-of-the-art canopy height or AGB products, a simple stocking index was derived from GEDI relative heights and TESSERA embeddings. This permits comparing state-of-the-art models often used in the voluntary carbon market with a TESSERA-derived stocking index.

To model a suitable stocking index from the 128-dimensional TESSERA embeddings, we extracted 110,000 relative heights RH95 and RH10 from the GEDI Level 4A product [53] from 2022 from the land area within the 22MCT Sentinel-2 tile in Para State, Brazil. From the 10 m pixel falling at the centre of each full-waveform footprint, the 128 TESSERA embeddings were extracted as predictor variables for regression analysis, with the relative height differences ( $dRH = RH95 - RH10$ ) used as the target variables. A random forest (RF) regression model with 500 trees and 42 variables per split was used to model this stocking index. The TerraClass Amazonia 2022 land cover map [117] was used to distinguish between forest and non-forest. To account for implausible GEDI recordings often found in areas without significant tree cover (e.g., water surfaces or agricultural fields), the  $dRH$  values of these classes were set to zero before model training.

### *Stocking index baselines*

For inference and assessment, the trained RF model was applied to eight Sentinel-2 tiles in the same region of Para State (MGRS tiles 22MCT, 22MCU, 22MDT, 22MDU, 22MGB, 22MGC, 22MHB, 22MHC). Within this area, a total of 38 agroforestry plots are located for which in situ measurements are available under a DTA. For comparison, five recent and widely used canopy height and AGB products were chosen and compared against the same set of 38 in situ AGB measurements: ETH CHM (10 m) [58], CTrees canopy tree height (5 m) [118], ESA-CCI AGB (100 m) [119], Meta CHM (1 m) [60], and GTDX AGB (25 m) [120]. Using the same TerraClass Amazonia 2022 shapefiles that define the agroforestry systems, the pixels of the respective products were extracted and averaged for the chronosequence plots ( $n=38$ ).

To ensure a fair comparison between canopy height, AGB and relative height products, the extracted averages were linearly rescaled to best correlate with in situ (AGB) data. After rescaling, all products are in units of t/ha and have an intercept of zero and a slope of one with respect to the in situ data, making their RMSE (and  $R^2$ ) directly comparable. The rescaling is as follows:

1. TESSERA: difference in relative heights of GEDI estimates of RH90 and RH10 converted to AGB using  $15.502 \times + 160.5$
2. ETH canopy height converted using  $3.4 \times$
3. CTrees canopy height converted using  $1.806 \times + 44.9$
4. ESA AGB converted using  $0.407 \times + 34.0$
5. Meta canopy height converted using  $3.723 \times + 46.6$
6. GEDI-Tandem-X AGB prediction converted using  $0.3 \times + 54.3$

## A.9 Interactive Habitat Mapping Tool

Here we demonstrate our interactive classification tool, a web-based utility designed for rapid human-in-the-loop habitat mapping using pre-computed model embeddings, as seen in Figure 14. The tool allows a user to first define a region of interest, for which it fetches and mosaics the relevant high-dimensional embedding tiles. To aid visual interpretation, it performs Principal Component Analysis on the embeddings

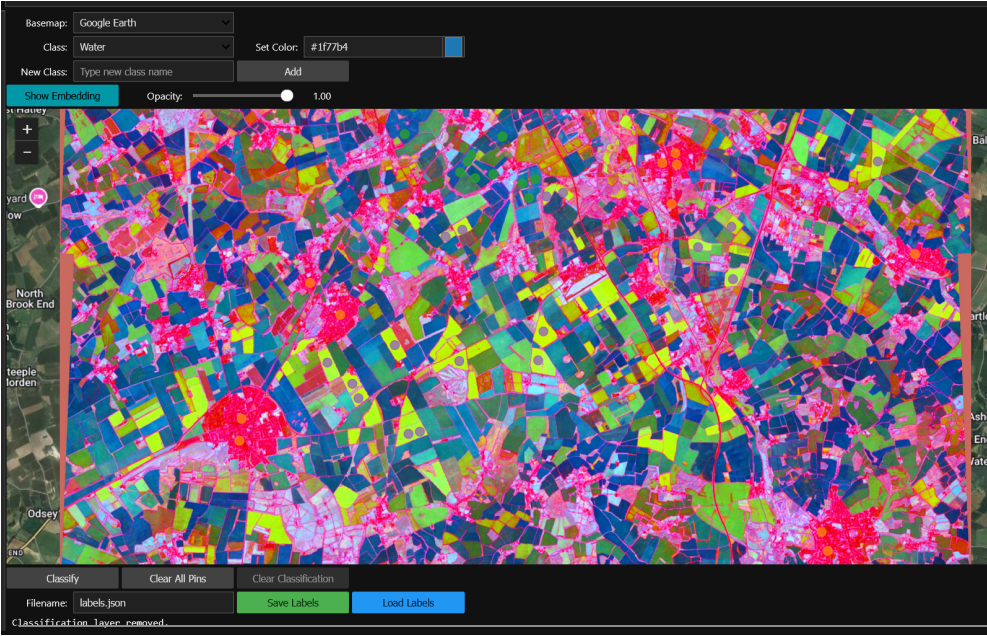


**Fig. 14** We provide an interactive tool to allow non-specialist users to map TESSERA embeddings to user-defined classes. We show a PCA-derived false colour map overlaid on an RGB aerial image of South Cambridge.

and displays the first three components as a false-colour RGB image overlay on a satellite basemap.

The core of the tool is the interactive labelling workflow. A user can define custom habitat classes and provide training data by clicking on the map to place labelled points. These points and their corresponding 128-dimensional embedding vectors are used to train a k-Nearest Neighbors (kNN) classifier. The trained model then predicts a class for every pixel in the region of interest, producing a map layer that overlays a coregistered aerial view. This process allows for iterative refinement, where a user can add more points to correct misclassifications and retrain the model for immediate feedback, demonstrating an accessible method for quickly creating habitat maps without requiring deep machine learning expertise. We also provide a batch processing tool for larger regions of interest. The tools and their open source code are freely available in our github repository [37].

**Table 5: TESSERA provides unprecedented ease of use, scale, and accuracy.** Unlike other remote sensing foundation models, TESSERA provides analysis-ready and gap-free outputs (R), is open (O), and provides global (G) annual (A) coverage at 10 m resolution (10 m). It uses spectral-temporal features (ST) at pixel level (P), is invariant to clouds (CI), provides a compressed representation (CR), is oriented to land features (LO), and includes both multispectral and radar information (MS). Codes:  $\checkmark$  = Yes,  $\times$  = No,  $\textcolor{brown}{?}$  = Unknown,  $\textcolor{orange}{p}$  = Potentially true,  $\textcolor{gray}{..}$  = N/A.

Foundation Model	R	O	G	A	10 m	ST	P	CI	CR	LO	MS
TESSERA (2025)	$\checkmark$	$\checkmark$	$\checkmark$	$\checkmark$	$\checkmark$	$\checkmark$	$\checkmark$	$\checkmark$	$\checkmark$	$\checkmark$	$\checkmark$
GeoKR (2021) [121]	$\times$	$\textcolor{brown}{?}$	$\times$	$\times$	$\checkmark$	$\times$	$\checkmark$	$\times$	$\times$	$\checkmark$	$\checkmark$
CVPRW (2021) [122]	$\times$	$\textcolor{gray}{..}$	$\times$	$\times$	$\checkmark$	$\times$	$\times$	$\times$	$\textcolor{gray}{..}$	$\checkmark$	$\times$
GASSL (2021) [23]	$\times$	$\textcolor{gray}{..}$	$\times$	$\times$	$\checkmark$	$\times$	$\checkmark$	$\times$	$\textcolor{gray}{..}$	$\checkmark$	$\times$
SeCo (2021) [123]	$\times$	$\times$	$\times$	$\times$	$\checkmark$	$\times$	$\times$	$\times$	$\textcolor{brown}{?}$	$\checkmark$	$\times$
MOSAIKS (2021) [124]	$\times$	$\checkmark$	$\checkmark$	$\times$	$\times$	$\times$	$\times$	$\times$	$\checkmark$	$\checkmark$	$\textcolor{brown}{?}$
DINO-MM (2022) [125]	$\times$	$\textcolor{gray}{..}$	$\times$	$\times$	$\checkmark$	$\times$	$\times$	$\times$	$\textcolor{gray}{..}$	$\checkmark$	$\checkmark$
SatMAE (2022) [16]	$\times$	$\textcolor{gray}{..}$	$\times$	$\times$	$\checkmark$	$\checkmark$	$\times$	$\times$	$\textcolor{orange}{p}$	$\textcolor{gray}{..}$	$\textcolor{orange}{p}$
RS-BYOL (2022) [126]	$\times$	$\textcolor{gray}{..}$	$\textcolor{gray}{..}$	$\times$	$\checkmark$	$\times$	$\checkmark$	$\checkmark$	$\textcolor{gray}{..}$	$\times$	$\checkmark$
GeCo (2022) [127]	$\times$	$\textcolor{gray}{..}$	$\textcolor{gray}{..}$	$\times$	$\textcolor{gray}{..}$	$\times$	$\times$	$\times$	$\textcolor{gray}{..}$	$\textcolor{orange}{p}$	$\times$
RingMo (2022) [128]	$\times$	$\textcolor{gray}{..}$	$\textcolor{gray}{..}$	$\times$	$\checkmark$	$\times$	$\times$	$\times$	$\textcolor{brown}{?}$	$\checkmark$	$\times$
RVSA (2022) [129]	$\times$	$\textcolor{gray}{..}$	$\textcolor{gray}{..}$	$\times$	$\textcolor{gray}{..}$	$\times$	$\times$	$\times$	$\textcolor{gray}{..}$	$\checkmark$	$\times$
RSP (2022) [14]	$\times$	$\textcolor{gray}{..}$	$\textcolor{gray}{..}$	$\times$	$\textcolor{orange}{p}$	$\times$	$\times$	$\textcolor{orange}{p}$	$\checkmark$	$\checkmark$	$\times$
MATTER (2022) [130]	$\times$	$\textcolor{gray}{..}$	$\textcolor{gray}{..}$	$\times$	$\checkmark$	$\checkmark$	$\times$	$\times$	$\checkmark$	$\checkmark$	$\times$
CSPT (2022) [131]	$\times$	$\textcolor{gray}{..}$	$\textcolor{gray}{..}$	$\times$	$\textcolor{brown}{?}$	$\times$	$\times$	$\times$	$\checkmark$	$\checkmark$	$\times$
CVPRW (2022) [132]	$\times$	$\textcolor{gray}{..}$	$\textcolor{gray}{..}$	$\times$	$\checkmark$	$\times$	$\times$	$\times$	$\checkmark$	$\checkmark$	$\checkmark$
BFM (2023) [133]	$\times$	$\textcolor{gray}{..}$	$\textcolor{gray}{..}$	$\times$	$\textcolor{brown}{?}$	$\times$	$\times$	$\times$	$\textcolor{brown}{?}$	$\checkmark$	$\times$
TOV (2023) [134]	$\textcolor{brown}{?}$	$\textcolor{gray}{..}$	$\times$	$\times$	$\checkmark$	$\times$	$\textcolor{brown}{?}$	$\times$	$\textcolor{brown}{?}$	$\checkmark$	$\times$
CMID (2023) [135]	$\times$	$\textcolor{gray}{..}$	$\times$	$\times$	$\checkmark$	$\times$	$\times$	$\times$	$\textcolor{brown}{?}$	$\checkmark$	$\times$
RingMo-Sense (2023) [136]	$\times$	$\textcolor{gray}{..}$	$\times$	$\times$	$\checkmark$	$\checkmark$	$\times$	$\times$	$\textcolor{brown}{?}$	$\checkmark$	$\checkmark$
lal-SimCLR (2023) [137]	$\times$	$\textcolor{gray}{..}$	$\times$	$\times$	$\checkmark$	$\times$	$\times$	$\times$	$\checkmark$	$\checkmark$	$\checkmark$
CACo (2023) [138]	$\times$	$\textcolor{gray}{..}$	$\times$	$\times$	$\checkmark$	$\checkmark$	$\times$	$\times$	$\checkmark$	$\checkmark$	$\times$
SatLas (2023) [15]	$\times$	$\textcolor{gray}{..}$	$\checkmark$	$\times$	$\checkmark$	$\checkmark$	$\checkmark$	$\times$	$\checkmark$	$\checkmark$	$\times$
GFM (2023) [139]	$\times$	$\textcolor{gray}{..}$	$\times$	$\times$	$\checkmark$	$\times$	$\times$	$\times$	$\times$	$\checkmark$	$\times$
Scale-MAE (2023) [140]	$\times$	$\textcolor{gray}{..}$	$\times$	$\times$	$\checkmark$	$\times$	$\times$	$\times$	$\times$	$\checkmark$	$\times$
DINO-MC (2023) [141]	$\times$	$\textcolor{gray}{..}$	$\times$	$\times$	$\checkmark$	$\times$	$\times$	$\times$	$\times$	$\checkmark$	$\times$
CROMA (2023) [142]	$\times$	$\textcolor{gray}{..}$	$\times$	$\times$	$\checkmark$	$\times$	$\times$	$\times$	$\times$	$\checkmark$	$\checkmark$
Cross-Scale MAE (2023) [143]	$\times$	$\textcolor{gray}{..}$	$\times$	$\times$	$\checkmark$	$\times$	$\times$	$\times$	$\times$	$\checkmark$	$\times$
DeCUR (2023) [144]	$\times$	$\textcolor{gray}{..}$	$\times$	$\times$	$\checkmark$	$\times$	$\times$	$\checkmark$	$\times$	$\checkmark$	$\checkmark$
Presto (2023) [19]	$\times$	$\textcolor{gray}{..}$	$\checkmark$	$\checkmark$	$\checkmark$	$\checkmark$	$\checkmark$	$\checkmark$	$\checkmark$	$\checkmark$	$\checkmark$
CtxMIM (2023) [145]	$\times$	$\textcolor{gray}{..}$	$\times$	$\times$	$\checkmark$	$\times$	$\times$	$\times$	$\times$	$\checkmark$	$\times$
FG-MAE (2023) [146]	$\times$	$\textcolor{gray}{..}$	$\times$	$\times$	$\checkmark$	$\times$	$\times$	$\times$	$\times$	$\checkmark$	$\times$
Prithvi (2023) [17]	$\times$	$\textcolor{gray}{..}$	$\times$	$\times$	$\textcolor{gray}{..}$	$\checkmark$	$\times$	$\checkmark$	$\checkmark$	$\checkmark$	$\times$

Continued on next page

Foundation Model	R	O	G	A	10 m	ST	P	CI	CR	LO	MS
RingMo-Lite (2023) [147]	✗	..	✗	✗	✓	✗	✗	✗	✗	✓	✗
IGARSS (2023) [148]	✗	..	✗	✗	✓	✗	✗	✗	✗	✓	✗
EarthPTi (2023) [149]	✗	..	✗	✗	✓	✓	✓	✓	✓	✓	✗
USat (2023) [150]	✗	..	✗	✗	✓	✗	✗	✗	✗	✓	✗
AIEarth (2023) [151]	p	?	✓	✗	✓	✗	✗	✗	✗	✓	✗
Clay (2023) [152]	✗	..	✓	✗	✓	✗	✗	✗	✗	✓	✗
Hydro (2023) [153]	✗	..	✗	✗	✓	✗	✗	✗	✗	✗	✗
U-Barn (2023) [154]	✗	..	✗	✓	✓	✓	✗	✓	✗	✓	✗
GeRSP (2023) [155]	✗	..	✗	✗	✓	✗	✗	✗	✗	✓	✗
SwiMDiff (2023) [156]	✗	..	✗	✗	✓	✗	✗	✗	✗	✓	✗
OFA-Net (2023) [157]	✗	..	✓	✗	✓	✗	✗	✗	✗	✓	✓
SML-FR (2023) [158]	p	p	✓	✗	✓	✗	✗	✗	✗	✗	✗
Spectral-GP (2024) [18]	✗	✗	✓	✗	✓	✗	✗	✗	✗	✓	✗
S2MAE (2024) [159]	✗	✗	✓	✗	✓	✗	✗	✗	✗	✓	✗
SatMAE++ (2024) [160]	✗	✗	✓	✗	✓	✗	✗	✗	✗	✓	✗
msGFM (2024) [161]	✗	✗	✗	✗	✓	✗	✗	✗	✗	✓	✗
SkySense (2024) [24]	✗	✗	✗	✗	✓	✓	✗	✗	✗	✓	✓
MTP (2024) [162]	✗	..	✓	✗	✓	✗	✓	✗	✗	✓	✗
DOFA (2024) [163]	✗	..	✓	✗	✓	✗	✗	✗	✓	✓	✓
MMEarth (2024) [164]	✗	..	✓	✗	✓	✗	✗	✗	✓	✓	✓
LeMeViT (2024) [165]	✗	..	✗	✗	?	✗	✗	✗	✓	✗	✗
SoftCon (2024) [166]	✗	..	✓	✗	✓	✗	✓	✗	✗	✓	✗
RS-DFM (2024) [167]	✗	..	✗	✗	✓	✗	✓	✗	✗	✓	✗
A2MAE (2024) [168]	✗	..	✓	✗	✓	✗	✗	✗	✓	✓	✗
HyperSIGM (2024) [169]	✗	..	✓	✗	✓	✓	✓	✗	✓	✓	✗
SelectiveMAE (2024) [170]	✗	..	✓	✗	✓	✗	✗	✗	✓	✓	✗
OmniSat (2024) [171]	✗	..	✗	✓	✓	✓	✓	✗	?	✓	✓
MM-VSE (2024) [172]	✗	..	✓	✓	✓	✓	✓	✗	?	✓	✓
MA3E (2024) [173]	✗	..	✗	✗	✓	✗	✗	✗	✓	✓	✗
SpectralEarth (2024) [174]	✗	..	✓	✓	✗	?	✓	✗	✓	✓	✗
SenPa-MAE (2024) [175]	✗	..	✓	✓	✓	✓	✓	✓	✗	✓	✗
RingMo-Ae (2024) [176]	✗	..	✗	✗	✓	✗	✓	✗	✓	✓	✗
SAR-JEPA (2024) [177]	✗	..	✗	✗	✓	✗	✗	✓	✗	✗	✗
PIS (2024) [178]	✗	?	✓	✓	✓	..	..	..	..	..	..
OREole-FM (2024) [179]	✗	..	✓	✗	✓	✗	✓	✗	✓	✓	✗
PIEVIT (2024) [180]	✗	..	✓	✗	✓	✗	✓	✗	✓	✓	✗
SatVisionTOA (2024) [181]	✗	..	✓	✓	✗	✓	✓	✓	✓	✓	✗
RS-vHeat (2024) [182]	✗	..	?	?	?	?	✓	?	✓	?	✓
Prithvi-EO-2.0 (2024) [110]	✗	..	✓	✓	✗	✓	✗	✓	✓	✓	✗
AnySat (2024) [183]	✗	..	✓	✗	✓	✗	✓	✗	✓	✓	✓
WildSAT (2024) [184]	✗	✗	✗	✗	✗	✗	✗	✗	✓	✓	✗
SeaMo (2024) [185]	✗	✗	✗	✗	✓	✗	✗	✗	✓	✓	✗
FoMo (2025) [186]	✓	✓	✓	✗	✓	✗	✓	✗	✓	✓	✓

Continued on next page

Foundation Model	R	O	G	A	10 m	ST	P	CI	CR	LO	MS
SatMamba (2025) [187]	✓	✓	✗	✗	✗	✗	✗	✗	✗	✓	✗
Galileo (2025) [188]	p	p	✓	?	✓	✗	?	?	✓	✓	✓
SatDiFuser (2025)[189]	✗	✗	✗	✗	✓	✗	✗	✗	✗	✓	✗
RoMA (2025) [190]	✗	✗	✗	✗	✓	✗	✗	✗	✗	✓	✗
Panopticon (2025) [191]	✗	✓	✗	✗	✓	✓	✗	✗	✓	✓	✓
FedSense (2025) [192]	✗	✗	✗	✗	✗	✗	✗	✗	✗	✓	✗
Copernicus-FM (2025) [193]	✗	..	✓	✗	✓	✓	✗	✗	✓	✓	✓
HyperFree (2025) [194]	✗	..	✗	✗	✓	✗	✗	✗	✓	✓	✗
DynamicVis (2025) [195]	✗	..	✗	✗	✓	✗	✗	✗	✗	✓	✓
FlexiMo (2025) [196]	✗	..	✗	✗	✓	✗	✗	✗	✗	✓	✓
Google Satellite (2025)[39]	✓	✗	✓	✓	✓	✓	✓	✓	✓	✓	✓
SkySense++ (2025) [197]	✗	✓	✓	p	p	✓	✗	p	✓	✓	✓
RingMoE (2025) [198]	✗	..	✗	✗	✓	✓	✗	✗	✓	✓	✓

## References

- [1] Pettorelli, N. *et al.* Satellite remote sensing of ecosystem functions: opportunities, challenges and way forward. *Remote Sensing in Ecology and Conservation* **4**, 71–93 (2018).
- [2] Yan, Y. *et al.* Satellite-based evidence of recent decline in global forest recovery rate from tree mortality events. *Nature Plants* 1–12 (2025).
- [3] Butler, D. Earth observation enters next phase. *Nature* **508**, 160–161 (2014).
- [4] Willett, D. S. *et al.* Noaa open data dissemination: Petabyte-scale earth system data in the cloud. *Science Advances* **9**, eadh0032 (2023).
- [5] Lisaius, M. C., Blake, A., Keshav, S. & Atzberger, C. Using barlow twins to create representations from cloud-corrupted remote sensing time series. *IEEE Journal of Selected Topics in Applied Earth Observations and Remote Sensing* **17**, 13162–13168 (2024).
- [6] Zhu, Z. Change detection using landsat time series: A review of frequencies, preprocessing, algorithms, and applications. *ISPRS Journal of Photogrammetry and Remote Sensing* **130**, 370–384 (2017).
- [7] Gómez, C., White, J. C. & Wulder, M. A. Optical remotely sensed time series data for land cover classification: A review. *ISPRS Journal of Photogrammetry and Remote Sensing* **116**, 55–72 (2016). URL <https://www.sciencedirect.com/science/article/pii/S0924271616000769>.
- [8] Roy, D. P. *et al.* Landsat-8: Science and product vision for terrestrial global change research. *Remote Sensing of Environment* **145**, 154–172 (2014).

[9] Corbane, C. *et al.* A global cloud free pixel- based image composite from sentinel-2 data. *Data in Brief* **31**, 105737 (2020). URL <https://www.sciencedirect.com/science/article/pii/S2352340920306314>.

[10] Amani, M. *et al.* Application of google earth engine cloud computing platform, sentinel imagery, and neural networks for crop mapping in canada. *Remote Sensing* **12** (2020). URL <https://www.mdpi.com/2072-4292/12/21/3561>.

[11] Xiao, A. *et al.* Foundation models for remote sensing and earth observation: A survey (2025). URL <https://arxiv.org/abs/2410.16602>. 2410.16602.

[12] Bodnar, C. *et al.* A foundation model for the earth system. *Nature* **641**, 1180–1187 (2025).

[13] Bi, K. *et al.* Accurate medium-range global weather forecasting with 3d neural networks. *Nature* **619**, 533–538 (2023).

[14] Wang, D., Zhang, J., Du, B., Xia, G.-S. & Tao, D. An empirical study of remote sensing pretraining. *IEEE Transactions on Geoscience and Remote Sensing* **61**, 1–20 (2023).

[15] Bastani, F., Wolters, P., Gupta, R., Ferdinando, J. & Kembhavi, A. *SatlasPretrain: A Large-Scale Dataset for Remote Sensing Image Understanding* , 16726–16736 (IEEE Computer Society, Los Alamitos, CA, USA, 2023). URL <https://doi.ieeecomputersociety.org/10.1109/ICCV51070.2023.01538>.

[16] Cong, Y. *et al.* *Satmae: pre-training transformers for temporal and multi-spectral satellite imagery*, NIPS '22 (Curran Associates Inc., Red Hook, NY, USA, 2022).

[17] Schmude, J. *et al.* Prithvi wxc: Foundation model for weather and climate (2024). URL <https://arxiv.org/abs/2409.13598>. 2409.13598.

[18] Hong, D. *et al.* Spectralgpt: Spectral remote sensing foundation model. *IEEE Transactions on Pattern Analysis and Machine Intelligence* **46**, 5227–5244 (2024). URL <http://dx.doi.org/10.1109/TPAMI.2024.3362475>.

[19] Tseng, G. *et al.* Lightweight, Pre-trained Transformers for Remote Sensing Timeseries (2024). URL <http://arxiv.org/abs/2304.14065>. ArXiv:2304.14065 [cs].

[20] Zheng, Z., Ermon, S., Kim, D., Zhang, L. & Zhong, Y. Changen2: Multi-temporal remote sensing generative change foundation model. *IEEE Transactions on Pattern Analysis and Machine Intelligence* **47**, 725–741 (2025).

[21] Khanna, S. *et al.* *Diffusionsat: A generative foundation model for satellite imagery* (2024). URL <https://openreview.net/forum?id=I5webNFDgQ>.

- [22] Pang, L., Tang, D., Xu, S., Meng, D. & Cao, X. Hsigene: A foundation model for hyperspectral image generation (2024). URL <https://arxiv.org/abs/2409.12470>. [2409.12470](https://arxiv.org/abs/2409.12470).
- [23] Ayush, K. *et al.* *Geography-aware self-supervised learning*, 10161–10170 (2021).
- [24] Guo, X. *et al.* *Skysense: A multi-modal remote sensing foundation model towards universal interpretation for earth observation imagery*, 27662–27673 (2024).
- [25] Huynh, A. V. *et al.* in *Contrastive ground-level image and remote sensing pre-training improves representation learning for natural world imagery* (eds Leonardis, A. *et al.*) *Computer Vision – ECCV 2024*, Vol. 15138 of *Lecture Notes in Computer Science* 10 (Springer, Cham, 2025).
- [26] Wang, Y. *et al.* Ssl4eo-s12: A large-scale multi-modal, multi-temporal dataset for self-supervised learning in earth observation. *ArXiv* **abs/2211.07044** (2022). URL <https://api.semanticscholar.org/CorpusID:253510090>.
- [27] Wang, D. *et al.* *Samrs: Scaling-up remote sensing segmentation dataset with segment anything model*, Vol. 36, 8815–8827 (2023).
- [28] Xiao, A. *et al.* Cat-sam: Conditional tuning for few-shot adaptation of segment anything model. *arXiv preprint arXiv:2402.03631* (2024).
- [29] Yan, Z. *et al.* Ringmo-sam: A foundation model for segment anything in multimodal remote-sensing images. *IEEE Transactions on Geoscience and Remote Sensing* **61**, 1–16 (2023).
- [30] Chen, K. *et al.* Rsprompter: Learning to prompt for remote sensing instance segmentation based on visual foundation model. *IEEE Transactions on Geoscience and Remote Sensing* (2024).
- [31] Zhang, X., Liu, Y., Lin, Y., Liao, Q. & Li, Y. *Uv-sam: adapting segment anything model for urban village identification*, AAAI'24/IAAI'24/EAAI'24 (AAAI Press, 2024). URL <https://doi.org/10.1609/aaai.v38i20.30260>.
- [32] Balestriero, R. *et al.* A cookbook of self-supervised learning (2023). URL <https://arxiv.org/abs/2304.12210>. [2304.12210](https://arxiv.org/abs/2304.12210).
- [33] Liu, X. *et al.* Self-supervised learning: Generative or contrastive. *IEEE Transactions on Knowledge and Data Engineering* 1–1 (2021). URL <http://dx.doi.org/10.1109/TKDE.2021.3090866>.
- [34] Zbontar, J., Jing, L., Misra, I., LeCun, Y. & Deny, S. Barlow twins: Self-supervised learning via redundancy reduction. *ArXiv* **abs/2103.03230** (2021).

[35] Barlow, H. B. Redundancy reduction revisited. *Network: Computation in Neural Systems* **12**, 241 – 253 (2001). URL <https://api.semanticscholar.org/CorpusID:18767856>.

[36] Wilkinson, M. D. *et al.* The fair guiding principles for scientific data management and stewardship. *Scientific Data* **3** (2016). URL <http://dx.doi.org/10.1038/SDATA.2016.18>.

[37] University of Cambridge Centre for Earth Observation. Ucam-*eo* project. [https://github.com/ucam-\*eo\*](https://github.com/ucam-eo). Accessed: 2025-07-22.

[38] Materials and methods are available as supplementary material.

[39] Brown, C. F. *et al.* Alphaearth foundations: An embedding field model for accurate and efficient global mapping from sparse label data (2025). URL <https://arxiv.org/abs/2507.22291>. [2507.22291](https://arxiv.org/abs/2507.22291).

[40] Weiss, M., Jacob, F. & Duveiller, G. Remote sensing for agricultural applications: A meta-review. *Remote Sensing of Environment* **236**, 111402 (2020).

[41] Ok, A. O., , A., Ozlem, & Gungor, O. Evaluation of random forest method for agricultural crop classification. *European Journal of Remote Sensing* **45**, 421–432 (2012). URL <https://doi.org/10.5721/EuJRS20124535>. Publisher: Taylor & Francis \_eprint: <https://doi.org/10.5721/EuJRS20124535>.

[42] Adegun, A. A., Viriri, S. & Tapamo, J.-R. Review of deep learning methods for remote sensing satellite images classification: experimental survey and comparative analysis. *Journal of Big Data* **10**, 93 (2023). URL <https://doi.org/10.1186/s40537-023-00772-x>.

[43] Joshi, A., Pradhan, B., Gite, S. & Chakraborty, S. Remote-Sensing Data and Deep-Learning Techniques in Crop Mapping and Yield Prediction: A Systematic Review. *Remote Sensing* **15**, 2014 (2023). URL <https://www.mdpi.com/2072-4292/15/8/2014>. Number: 8 Publisher: Multidisciplinary Digital Publishing Institute.

[44] INVEKOS Schläge Österreich 2022 - Open Government Data Austria. URL <https://www.data.gov.at/katalog/dataset/3ee31e14-a6ac-4fc6-913a-1a83995aec5a>.

[45] McInnes, L., Healy, J. & Melville, J. Umap: Uniform manifold approximation and projection for dimension reduction. *arXiv preprint arXiv:1802.03426* (2018).

[46] Mitchell, A. L., Rosenqvist, A. & Mora, B. Current remote sensing approaches to monitoring forest degradation in support of countries measurement, reporting and verification (MRV) systems for REDD+. *Carbon Balance and Management*

12, 9 (2017).

- [47] Feldpausch, T. R. *et al.* Tree height integrated into pantropical forest biomass estimates. *Biogeosciences* **9**, 3381–3403 (2012).
- [48] Migliavacca, M. *et al.* The three major axes of terrestrial ecosystem function. *Nature* **598**, 468–472 (2021).
- [49] Davies, A. B. & Asner, G. P. Advances in animal ecology from 3D-LiDAR ecosystem mapping. *Trends in Ecology & Evolution* **29**, 681–691 (2014).
- [50] Cazzolla Gatti, R., Di Paola, A., Bombelli, A., Noce, S. & Valentini, R. Exploring the relationship between canopy height and terrestrial plant diversity. *Plant Ecology* **218**, 899–908 (2017).
- [51] Skidmore, A. K. *et al.* Priority list of biodiversity metrics to observe from space. *Nature Ecology & Evolution* **5**, 896–906 (2021).
- [52] Borghi, C., Francini, S., D’Amico, G., Valbuena, R. & Chirici, G. Advancements in forest monitoring: Applications and perspectives of airborne laser scanning and complementarity with satellite optical data. *Land* **14**, 567 (2025).
- [53] Dubayah, R. *et al.* The Global Ecosystem Dynamics Investigation: High-resolution laser ranging of the Earth’s forests and topography. *Science of Remote Sensing* **1**, 100002 (2020).
- [54] Fu, L. *et al.* Accuracy assessment of topography and forest canopy height in complex terrain conditions of Southern China using ICESat-2 and GEDI data. *Frontiers in Plant Science* **16** (2025).
- [55] Sadeghi, Y., St-Onge, B., Leblon, B. & Simard, M. Canopy height model (chm) derived from a tandem-x insar dsm and an airborne lidar dtm in boreal forest. *IEEE Journal of Selected Topics in Applied Earth Observations and Remote Sensing* **9**, 381–397 (2016).
- [56] Wang, C. *et al.* Interpretable Multi-Sensor Fusion of Optical and SAR Data for GEDI-Based Canopy Height Mapping in Southeastern North Carolina. *Remote Sensing* **17**, 1536 (2025).
- [57] Liu, A., Chen, Y. & Cheng, X. Improving Tropical Forest Canopy Height Mapping by Fusion of Sentinel-1/2 and Bias-Corrected ICESat-2–GEDI Data. *Remote Sensing* **17**, 1968 (2025).
- [58] Lang, N., Jetz, W., Schindler, K. & Wegner, J. D. A high-resolution canopy height model of the Earth. *Nature Ecology & Evolution* **7**, 1778–1789 (2023).
- [59] Potapov, P. *et al.* Mapping global forest canopy height through integration of GEDI and Landsat data. *Remote Sensing of Environment* **253**, 112165 (2021).

- [60] Tolan, J. *et al.* Very high resolution canopy height maps from RGB imagery using self-supervised vision transformer and convolutional decoder trained on aerial lidar. *Remote Sensing of Environment* **300**, 113888 (2024).
- [61] Lahssini, K., Baghdadi, N., le Maire, G., Fayad, I. & Villard, L. Canopy height mapping in French Guiana using multi-source satellite data and environmental information in a U-Net architecture. *Frontiers in Remote Sensing* **5** (2024).
- [62] Moudrý, V. *et al.* Comparison of three global canopy height maps and their applicability to biodiversity modeling: Accuracy issues revealed. *Ecosphere* **15**, e70026 (2024).
- [63] Moudrý, V. *et al.* Harmonised airborne laser scanning products can address the limitations of large-scale spaceborne vegetation mapping (2024).
- [64] Pauls, J. *et al.* Capturing Temporal Dynamics in Large-Scale Canopy Tree Height Estimation. <https://arxiv.org/abs/2501.19328v1> (2025).
- [65] Jackson, T. D. *et al.* Tall Bornean forests experience higher canopy disturbance rates than those in the eastern Amazon or Guiana shield. *Global Change Biology* **30** (2024).
- [66] Coomes, D. & Jackson, T. Airborne LiDAR and RGB imagery from Sepilok Reserve and Danum Valley in Malaysia in 2020 (2022).
- [67] Rolf, E., Gordon, L., Tambe, M. & Davies, A. Contrasting local and global modeling with machine learning and satellite data: A case study estimating tree canopy height in African savannas (2024). [2411.14354](https://arxiv.org/abs/2411.14354).
- [68] Lang, N., Schindler, K. & Wegner, J. D. High carbon stock mapping at large scale with optical satellite imagery and spaceborne LIDAR (2021). [2107.07431](https://arxiv.org/abs/2107.07431).
- [69] Herold, M. *et al.* The role and need for space-based forest biomass-related measurements in environmental management and policy. *Surveys in Geophysics* **40** (2019).
- [70] Duncanson, L. *et al.* The importance of consistent validation of global forest aboveground biomass products. *Surveys in Geophysics* **40** (2019).
- [71] Zhao, Z., Dong, L., Wu, S., Xiao, X. *et al.* Review of remote sensing-based methods for forest aboveground biomass estimation: Progress, challenges, and prospects. *Forests* **14**, 1086 (2023).
- [72] Nascetti, A. *et al.* *Biomasssters: A benchmark dataset for forest biomass estimation using multi-modal satellite time-series* (2023). URL <https://openreview.net/forum?id=hrWsIC4Cmz>.

[73] The biomassters: Estimating aboveground biomass in finnish forests. <https://www.drivendata.org/competitions/99/biomass-estimation/> (2023). DrivenData competition website, accessed July 29, 2025.

[74] Repola, J. Biomass equations for birch in finland. *Silva Fennica* **42**, 605–624 (2008).

[75] Repola, J. Biomass equations for scots pine and norway spruce in finland. *Silva Fennica* **43**, 625–647 (2009).

[76] Ronneberger, O., Fischer, P. & Brox, T. U-Net: Convolutional Networks for Biomedical Image Segmentation (2015). [1505.04597](https://arxiv.org/abs/1505.04597).

[77] Sainte Fare Garnot, V. & Landrieu, L. *Lightweight temporal self-attention for classifying satellite images time series*, 171–181 (2020).

[78] Xiao, T., Liu, Y., Zhou, B., Jiang, Y. & Sun, J. *Unified perceptual parsing for scene understanding*, 418–434 (2018).

[79] Marsocci, V. *et al.* Pangaea: A global and inclusive benchmark for geospatial foundation models (2025). URL <https://arxiv.org/abs/2412.04204>. [2412.04204](https://arxiv.org/abs/2412.04204).

[80] Abatzoglou, J. T. & Williams, A. P. Impact of anthropogenic climate change on wildfire across western US forests. *Proceedings of the National Academy of Sciences* **113**, 11770–11775 (2016).

[81] Iglesias, V., Balch, J. K. & Travis, W. R. U.S. fires became larger, more frequent, and more widespread in the 2000s. *Science Advances* **8**, eabc0020 (2022).

[82] Pechony, O., Shindell, D. T. & Chapin, F. S. Driving forces of global wild-fires over the past millennium and the forthcoming century. *Proceedings of the National Academy of Sciences of the United States of America* **107**, 19167–19170 (2010).

[83] Andela, N. *et al.* A human-driven decline in global burned area. *Science* **356**, 1356–1362 (2017).

[84] Chen, Y., Morton, D. C., Andela, N., Giglio, L. & Randerson, J. T. How much global burned area can be forecast on seasonal time scales using sea surface temperatures? *Environ. Res. Lett.* **11**, 045001 (2016).

[85] Zang, J., Qiu, F. & Zhang, Y. A global dataset of forest regrowth following wildfires. *Sci Data* **11**, 1052 (2024).

[86] Hashida, Y., Lewis, D. J. & Cummins, K. Prescribed fires as a climate change adaptation tool. *Journal of Environmental Economics and Management* **130**, 103081 (2025).

[87] Kurbanov, E. *et al.* Remote Sensing of Forest Burnt Area, Burn Severity, and Post-Fire Recovery: A Review. *Remote Sensing* **14**, 4714 (2022).

[88] Picotte, J. J. *et al.* Changes to the Monitoring Trends in Burn Severity program mapping production procedures and data products. *Fire Ecology* **16**, 16 (2020).

[89] Hawbaker, T. J., Radeloff, V. C., Syphard, A. D., Zhu, Z. & Stewart, S. I. Detection rates of the MODIS active fire product in the United States. *Remote Sensing of Environment* **112**, 2656–2664 (2008).

[90] Hawbaker, T. J. *et al.* Mapping burned areas using dense time-series of Landsat data. *Remote Sensing of Environment* **198**, 504–522 (2017).

[91] Tanase, M. A. *et al.* Burned Area Detection and Mapping: Intercomparison of Sentinel-1 and Sentinel-2 Based Algorithms over Tropical Africa. *Remote Sensing* **12**, 334 (2020).

[92] Verhegghen, A. *et al.* The Potential of Sentinel Satellites for Burnt Area Mapping and Monitoring in the Congo Basin Forests. *Remote Sensing* **8**, 986 (2016).

[93] Chuvieco, E. *et al.* Historical background and current developments for mapping burned area from satellite Earth observation. *Remote Sensing of Environment* **225**, 45–64 (2019).

[94] Roteta, E., Bastarrika, A., Padilla, M., Storm, T. & Chuvieco, E. Development of a Sentinel-2 burned area algorithm: Generation of a small fire database for sub-Saharan Africa. *Remote Sensing of Environment* **222**, 1–17 (2019).

[95] Monitoring Trends in Burn Severity (ver. 12.0, April 2025) - ScienceBase-Catalog. <https://www.sciencebase.gov/catalog/item/5e541969e4b0ff554f753113>.

[96] Mutuo, P. K., Cadisch, G., Albrecht, A., Palm, C. & Verchot, L. Potential of agroforestry for carbon sequestration and mitigation of greenhouse gas emissions from soils in the tropics. *Nutrient cycling in Agroecosystems* **71**, 43–54 (2005).

[97] Verra. Vm0047 afforestation, reforestation, and revegetation, v1.1. <https://verra.org/methodologies/vm0047-afforestation-reforestation-and-revegetation-v1-1/> (2025). Verra Verified Carbon Standard (VCS) Program methodology.

[98] Atzberger, C. *et al.* A scalable, annual aboveground biomass product for monitoring carbon impacts of ecosystem restoration projects. *Remote Sensing of Environment* **327**, 114774 (2025). URL <https://www.sciencedirect.com/science/article/pii/S0034425725001786>.

[99] European Space Agency. Sentinel-2 data. Copernicus Data Space Ecosystem (2015–present). URL <https://dataspace.copernicus.eu/>.

- [100] European Space Agency. Sentinel-1 data. Copernicus Data Space Ecosystem (2014–present). URL <https://dataspace.copernicus.eu/>.
- [101] European Space Agency (ESA). SNAP - ESA Sentinel Application Platform (2024). URL <http://step.esa.int/main/toolboxes/snap/>.
- [102] Google LLC. Google Earth Engine: Planetary-scale geospatial analysis. Web page (2025). URL <https://earthengine.google.com>. Accessed: 2025-07-22.
- [103] Google LLC. Vertex AI: A fully-managed, end-to-end ML platform. Web page (2025). URL <https://cloud.google.com/vertex-ai>. Accessed: 2025-07-22.
- [104] Python Packaging Authority. Pypi - the python package index. <https://pypi.org/>. Accessed: 2025-07-22.
- [105] Harris, C. R. *et al.* Array programming with numpy. *Nature* **585**, 357–362 (2020).
- [106] Uieda, L. *et al.* Pooch: A friend to fetch your data files. *Journal of Open Source Software* **5**, 1943 (2020). URL <https://doi.org/10.21105/joss.01943>.
- [107] Vaswani, A. *et al.* *Attention is all you need*, NIPS’17, 6000–6010 (Curran Associates Inc., Red Hook, NY, USA, 2017).
- [108] Bandara, W. G. C., Melo, C. M. D. & Patel, V. M. Guarding barlow twins against overfitting with mixed samples (2023). URL <https://arxiv.org/abs/2312.02151>.
- [109] Garrido, Q., Balestriero, R., Najman, L. & Lecun, Y. *Rankme: Assessing the downstream performance of pretrained self-supervised representations by their rank*, 10929–10974 (PMLR, 2023).
- [110] Szwarcman, D. *et al.* Prithvi-eo-2.0: A versatile multi-temporal foundation model for earth observation applications (2025). URL <https://arxiv.org/abs/2412.02732>.
- [111] Shenkin, A. *et al.* The World’s Tallest Tropical Tree in Three Dimensions. *Front. For. Glob. Change* **2** (2019).
- [112] Piponiot, C. *et al.* Distribution of biomass dynamics in relation to tree size in forests across the world. *New Phytologist* **234**, 1664–1677 (2022).
- [113] Fischer, F. J., Jackson, T., Vincent, G. & Jucker, T. Robust characterisation of forest structure from airborne laser scanning—A systematic assessment and sample workflow for ecologists. *Methods in Ecology and Evolution* **15**, 1873–1888 (2024).

[114] Jakubik, J. *et al.* Foundation Models for Generalist Geospatial Artificial Intelligence (2023). [2310.18660](https://arxiv.org/abs/2310.18660).

[115] Dynamic World V1 | Earth Engine Data Catalog. [https://developers.google.com/earth-engine/datasets/catalog/GOOGLE\\_DYNAMICWORLD\\_V1](https://developers.google.com/earth-engine/datasets/catalog/GOOGLE_DYNAMICWORLD_V1).

[116] Giddey, B. L., Baard, J. A. & Kraaij, T. Verification of the differenced Normalised Burn Ratio (dNBR) as an index of fire severity in Afrotropical Forest. *South African Journal of Botany* **146**, 348–353 (2022).

[117] TerraClass. TerraClass: Mapeamento de uso e ocupação da terra. URL <https://terraclass.gov.br/>. Accessed: July 24, 2025.

[118] Wagner, F. H. *et al.* High resolution tree height mapping of the Amazon forest using Planet NICFI images and lidar-informed u-net model. *arXiv preprint arXiv:2501.10600* (2025). URL <https://arxiv.org/abs/2501.10600>.

[119] Santoro, M. & Cartus, O. Esa biomass climate change initiative (biomass\_cci): Global datasets of forest above-ground biomass for the years 2010, 2015, 2016, 2017, 2018, 2019, 2020 and 2021, v5.01 (2024). URL <https://doi.org/10.5285/BF535053562141C6BB7AD831F5998D77>.

[120] Dubayah, R. *et al.* Pantropical forest height and biomass from gedi and tandem-x data fusion (2023). URL <https://doi.org/10.3334/ORNLDAC/2298>.

[121] Li, W., Chen, K., Chen, H. & Shi, Z. Geographical knowledge-driven representation learning for remote sensing images. *IEEE Transactions on Geoscience and Remote Sensing* **60**, 1–16 (2022).

[122] Stojnic, V. & Risojevic, V. *Self-supervised learning of remote sensing scene representations using contrastive multiview coding*, 1182–1191 (2021).

[123] Mañas, O., Lacoste, A., Giró-i Nieto, X., Vazquez, D. & Rodríguez, P. *Seasonal contrast: Unsupervised pre-training from uncurated remote sensing data*, 9394–9403 (2021).

[124] Rolf, E. *et al.* A generalizable and accessible approach to machine learning with global satellite imagery. *Nature communications* **12**, 4392 (2021).

[125] Wang, Y., Albrecht, C. M. & Zhu, X. X. Self-supervised vision transformers for joint sar-optical representation learning (2022). URL <https://arxiv.org/abs/2204.05381>. [2204.05381](https://arxiv.org/abs/2204.05381).

[126] Jain, P., Schoen-Phelan, B. & Ross, R. Self-supervised learning for invariant representations from multi-spectral and sar images. *IEEE Journal of Selected Topics in Applied Earth Observations and Remote Sensing* **15**, 7797–7808 (2022).

- [127] Li, W., Chen, K. & Shi, Z. Geographical supervision correction for remote sensing representation learning. *IEEE Transactions on Geoscience and Remote Sensing* **60**, 1–20 (2022).
- [128] Sun, X. *et al.* Ringmo: A remote sensing foundation model with masked image modeling. *IEEE Transactions on Geoscience and Remote Sensing* **61**, 1–22 (2023).
- [129] Wang, D. *et al.* Advancing plain vision transformer toward remote sensing foundation model. *IEEE Transactions on Geoscience and Remote Sensing* **61**, 1–15 (2023).
- [130] Akiva, P., Purri, M. & Leotta, M. *Self-supervised material and texture representation learning for remote sensing tasks*, 8193–8205 (2022).
- [131] Zhang, T. *et al.* Consecutive pre-training: A knowledge transfer learning strategy with relevant unlabeled data for remote sensing domain. *Remote Sensing* **14** (2022). URL <https://www.mdpi.com/2072-4292/14/22/5675>.
- [132] Scheibenreif, L., Hanna, J., Mommert, M. & Borth, D. *Self-supervised vision transformers for land-cover segmentation and classification*, 1422–1431 (2022).
- [133] Cha, K., Seo, J. & Lee, T. A billion-scale foundation model for remote sensing images. *IEEE Journal of Selected Topics in Applied Earth Observations and Remote Sensing* 1–17 (2024). URL <http://dx.doi.org/10.1109/JSTARS.2024.3401772>.
- [134] Tao, C. *et al.* Tov: The original vision model for optical remote sensing image understanding via self-supervised learning. *IEEE Journal of Selected Topics in Applied Earth Observations and Remote Sensing* **16**, 4916–4930 (2023).
- [135] Muhtar, D., Zhang, X., Xiao, P., Li, Z. & Gu, F. Cmid: A unified self-supervised learning framework for remote sensing image understanding. *IEEE Transactions on Geoscience and Remote Sensing* **61**, 1–17 (2023).
- [136] Yao, F. *et al.* Ringmo-sense: Remote sensing foundation model for spatiotemporal prediction via spatiotemporal evolution disentangling. *IEEE Transactions on Geoscience and Remote Sensing* **61**, 1–21 (2023).
- [137] Prexl, J. & Schmitt, M. *Multi-modal multi-objective contrastive learning for sentinel-1/2 imagery*, 2136–2144 (2023).
- [138] Mall, U., Hariharan, B. & Bala, K. *Change-aware sampling and contrastive learning for satellite images*, 5261–5270 (2023).
- [139] Mendieta, M., Han, B., Shi, X., Zhu, Y. & Chen, C. *Towards geospatial foundation models via continual pretraining*, 16760–16770 (2023).

[140] Reed, C. J. *et al.* *Scale-MAE: A Scale-Aware Masked Autoencoder for Multiscale Geospatial Representation Learning* , 4065–4076 (IEEE Computer Society, Los Alamitos, CA, USA, 2023). URL <https://doi.ieeecomputersociety.org/10.1109/ICCV51070.2023.00378>.

[141] Wanyan, X., Seneviratne, S., Shen, S. & Kirley, M. Extending global-local view alignment for self-supervised learning with remote sensing imagery (2024). URL <https://arxiv.org/abs/2303.06670>. 2303.06670.

[142] Fuller, A., Millard, K. & Green, J. Croma: Remote sensing representations with contrastive radar-optical masked autoencoders. *Advances in Neural Information Processing Systems* **36**, 5506–5538 (2023).

[143] Tang, M., Cozma, A., Georgiou, K. & Qi, H. *Cross-scale mae: a tale of multi-scale exploitation in remote sensing*, NIPS '23 (Curran Associates Inc., Red Hook, NY, USA, 2023).

[144] Wang, Y. *et al.* Decoupling common and unique representations for multimodal self-supervised learning (2024). URL <https://arxiv.org/abs/2309.05300>. 2309.05300.

[145] Zhang, M., Liu, Q. & Wang, Y. Ctxmim: Context-enhanced masked image modeling for remote sensing image understanding (2024). URL <https://arxiv.org/abs/2310.00022>. 2310.00022.

[146] Wang, Y., Hernández, H. H., Albrecht, C. M. & Zhu, X. X. Feature guided masked autoencoder for self-supervised learning in remote sensing (2023). URL <https://arxiv.org/abs/2310.18653>. 2310.18653.

[147] Wang, Y. *et al.* Ringmo-lite: A remote sensing multi-task lightweight network with cnn-transformer hybrid framework (2023). URL <https://arxiv.org/abs/2309.09003>. 2309.09003.

[148] Feng, Y. *et al.* *A self-supervised cross-modal remote sensing foundation model with multi-domain representation and cross-domain fusion*, 2239–2242 (2023).

[149] Smith, M. J., Fleming, L. & Geach, J. E. Earthpt: a time series foundation model for earth observation (2024). URL <https://arxiv.org/abs/2309.07207>. 2309.07207.

[150] Irvin, J. *et al.* Usat: A unified self-supervised encoder for multi-sensor satellite imagery (2023). URL <https://arxiv.org/abs/2312.02199>. 2312.02199.

[151] Xu, H. *et al.* Analytical insight of earth: A cloud-platform of intelligent computing for geospatial big data (2023). URL <https://arxiv.org/abs/2312.16385>. 2312.16385.

- [152] Clay Foundation Team. Clay foundation model: An open source ai model and interface for earth. <https://madewithclay.org> (2023). Version 0.0.1, Apache License, code and model weights available on GitHub and Hugging Face.
- [153] Corley, I. & Robinson, C. Hydro foundation model. <https://github.com/isaaccorley/hydro-foundation-model> (2024).
- [154] Dumeur, I., Valero, S. & Inglada, J. Self-supervised spatio-temporal representation learning of satellite image time series. *IEEE Journal of Selected Topics in Applied Earth Observations and Remote Sensing* **17**, 4350–4367 (2024).
- [155] Huang, Z., Zhang, M., Gong, Y., Liu, Q. & Wang, Y. Generic knowledge boosted pretraining for remote sensing images. *IEEE Transactions on Geoscience and Remote Sensing* **62**, 1–13 (2024).
- [156] Tian, J., Lei, J., Zhang, J., Xie, W. & Li, Y. Swimdiff: Scene-wide matching contrastive learning with diffusion constraint for remote sensing image (2024). URL <https://arxiv.org/abs/2401.05093>. **2401.05093**.
- [157] Xiong, Z., Wang, Y., Zhang, F. & Zhu, X. X. One for all: Toward unified foundation models for earth vision (2024). URL <https://arxiv.org/abs/2401.07527>. **2401.07527**.
- [158] Dong, Z., Gu, Y. & Liu, T. Generative convnet foundation model with sparse modeling and low-frequency reconstruction for remote sensing image interpretation. *IEEE Transactions on Geoscience and Remote Sensing* **62**, 1–16 (2024).
- [159] Li, X., Hong, D. & Chanussot, J. *S2mae: A spatial-spectral pretraining foundation model for spectral remote sensing data*, 24088–24097 (2024).
- [160] Noman, M. *et al.* *Rethinking Transformers Pre-training for Multi-Spectral Satellite Imagery* , 27811–27819 (IEEE Computer Society, Los Alamitos, CA, USA, 2024). URL <https://doi.ieeecomputersociety.org/10.1109/CVPR52733.2024.02627>.
- [161] Han, B., Zhang, S., Shi, X. & Reichstein, M. *Bridging remote sensors with multisensor geospatial foundation models*, 27852–27862 (2024).
- [162] Wang, D. *et al.* Mtp: Advancing remote sensing foundation model via multi-task pretraining (2024). URL <https://arxiv.org/abs/2403.13430>. **2403.13430**.
- [163] Xiong, Z. *et al.* Neural plasticity-inspired multimodal foundation model for earth observation (2024). URL <https://arxiv.org/abs/2403.15356>. **2403.15356**.
- [164] Nedungadi, V. *et al.* Leonardis, A. *et al.* (eds) *Mmearth: Exploring multi-modal pretext tasks for geospatial representation learning*. (eds Leonardis, A.

*et al.) Computer Vision - ECCV 2024 - 18th European Conference, Milan, Italy, September 29-October 4, 2024, Proceedings, Part LXIV, Vol. 15122 of Lecture Notes in Computer Science, 164–182 (Springer, 2024). URL [https://doi.org/10.1007/978-3-031-73039-9\\_10](https://doi.org/10.1007/978-3-031-73039-9_10).*

- [165] Jiang, W. *et al.* Lemevit: Efficient vision transformer with learnable meta tokens for remote sensing image interpretation (2024). URL <https://arxiv.org/abs/2405.09789>. **2405.09789**.
- [166] Wang, Y., Albrecht, C. M. & Zhu, X. X. Multilabel-guided soft contrastive learning for efficient earth observation pretraining. *IEEE Transactions on Geoscience and Remote Sensing* **62**, 1–16 (2024).
- [167] Wang, Z. *et al.* Rs-dfm: A remote sensing distributed foundation model for diverse downstream tasks (2024). URL <https://arxiv.org/abs/2406.07032>. **2406.07032**.
- [168] Zhang, L. *et al.* A<sup>2</sup>-mae: A spatial-temporal-spectral unified remote sensing pre-training method based on anchor-aware masked autoencoder (2024). URL <https://arxiv.org/abs/2406.08079>. **2406.08079**.
- [169] Wang, D. *et al.* Hypersigma: Hyperspectral intelligence comprehension foundation model (2025). URL <https://arxiv.org/abs/2406.11519>. **2406.11519**.
- [170] Wang, F. *et al.* Harnessing massive satellite imagery with efficient masked image modeling (2025). URL <https://arxiv.org/abs/2406.11933>. **2406.11933**.
- [171] Astruc, G., Gonthier, N., Mallet, C. & Landrieu, L. *Omnisat: Self-supervised modality fusion for earth observation*, 409–427 (Springer, 2024).
- [172] Ravirathinam, P., Khandelwal, A., Ghosh, R. & Kumar, V. A causally informed pretraining approach for multimodal foundation models: Applications in remote sensing. *arXiv preprint arXiv:2407.19660* (2024).
- [173] Li, Z. *et al.* *Masked angle-aware autoencoder for remote sensing images*, 260–278 (Springer, 2025).
- [174] Li, Z. *et al.* Masked angle-aware autoencoder for remote sensing images (2024). URL <https://arxiv.org/abs/2408.01946>. **2408.01946**.
- [175] Prexl, J. & Schmitt, M. Senpa-mae: Sensor parameter aware masked autoencoder for multi-satellite self-supervised pretraining (2024). URL <https://arxiv.org/abs/2408.11000>. **2408.11000**.
- [176] Diao, W. *et al.* Ringmo-aerial: An aerial remote sensing foundation model with affine transformation contrastive learning (2025). URL <https://arxiv.org/abs/2409.13366>. **2409.13366**.

[177] Li, W. *et al.* Predicting gradient is better: Exploring self-supervised learning for sar atr with a joint-embedding predictive architecture. *ISPRS Journal of Photogrammetry and Remote Sensing* **218**, 326–338 (2024). URL <https://www.sciencedirect.com/science/article/pii/S0924271624003514>.

[178] An, X., He, W., Zou, J., Yang, G. & Zhang, H. Pretrain a remote sensing foundation model by promoting intra-instance similarity. *IEEE Transactions on Geoscience and Remote Sensing* **62**, 1–15 (2024).

[179] Dias, P. *et al.* *Oreole-fm: successes and challenges toward billion-parameter foundation models for high-resolution satellite imagery*, SIGSPATIAL '24, 597–600 (ACM, 2024). URL <http://dx.doi.org/10.1145/3678717.3691292>.

[180] Lu, K. *et al.* Pattern integration and enhancement vision transformer for self-supervised learning in remote sensing. *IEEE Transactions on Geoscience and Remote Sensing* (2025).

[181] Spradlin, C. S. *et al.* Satvision-toa: A geospatial foundation model for coarse-resolution all-sky remote sensing imagery (2024). URL <https://arxiv.org/abs/2411.17000>. [2411.17000](https://arxiv.org/abs/2411.17000).

[182] Hu, H. *et al.* Rs-vheat: Heat conduction guided efficient remote sensing foundation model (2025). URL <https://arxiv.org/abs/2411.17984>. [2411.17984](https://arxiv.org/abs/2411.17984).

[183] Astruc, G., Gonthier, N., Mallet, C. & Landrieu, L. Anysat: One earth observation model for many resolutions, scales, and modalities (2025). URL <https://arxiv.org/abs/2412.14123>. [2412.14123](https://arxiv.org/abs/2412.14123).

[184] Daroya, R., Cole, E., Aodha, O. M., Horn, G. V. & Maji, S. Wildsat: Learning satellite image representations from wildlife observations (2024). URL <https://arxiv.org/abs/2412.14428>. [2412.14428](https://arxiv.org/abs/2412.14428).

[185] Li, X., Li, C., Vivone, G. & Hong, D. Seamo: A season-aware multimodal foundation model for remote sensing (2025). URL <https://arxiv.org/abs/2412.19237>. [2412.19237](https://arxiv.org/abs/2412.19237).

[186] Bountos, N. I., Ouaknine, A., Papoutsis, I. & Rolnick, D. Fomo: Multi-modal, multi-scale and multi-task remote sensing foundation models for forest monitoring (2025). URL <https://arxiv.org/abs/2312.10114>. [2312.10114](https://arxiv.org/abs/2312.10114).

[187] Duc, C. M. & Fukui, H. Satmamba: Development of foundation models for remote sensing imagery using state space models (2025). URL <https://arxiv.org/abs/2502.00435>. [2502.00435](https://arxiv.org/abs/2502.00435).

[188] Tseng, G. *et al.* Galileo: Learning global & local features of many remote sensing modalities (2025). URL <https://arxiv.org/abs/2502.09356>. [2502.09356](https://arxiv.org/abs/2502.09356).

- [189] Jia, Y. *et al.* Can generative geospatial diffusion models excel as discriminative geospatial foundation models? (2025). URL <https://arxiv.org/abs/2503.07890>. [2503.07890](https://arxiv.org/abs/2503.07890).
- [190] Wang, F. *et al.* Roma: Scaling up mamba-based foundation models for remote sensing (2025). URL <https://arxiv.org/abs/2503.10392>. [2503.10392](https://arxiv.org/abs/2503.10392).
- [191] Waldmann, L. *et al.* Panopticon: Advancing any-sensor foundation models for earth observation (2025). URL <https://arxiv.org/abs/2503.10845>. [2503.10845](https://arxiv.org/abs/2503.10845).
- [192] Tan, J., Zhang, C., Dang, B. & Li, Y. Towards privacy-preserved pre-training of remote sensing foundation models with federated mutual-guidance learning. *arXiv preprint arXiv:2503.11051* (2025).
- [193] Wang, Y. *et al.* Towards a unified copernicus foundation model for earth vision (2025). URL <https://arxiv.org/abs/2503.11849>. [2503.11849](https://arxiv.org/abs/2503.11849).
- [194] Li, J. *et al.* *Hyperfree: A channel-adaptive and tuning-free foundation model for hyperspectral remote sensing imagery* (2025).
- [195] Chen, K. *et al.* Dynamicvis: An efficient and general visual foundation model for remote sensing image understanding (2025). URL <https://arxiv.org/abs/2503.16426>. [2503.16426](https://arxiv.org/abs/2503.16426).
- [196] Li, X., Li, C., Ghamisi, P. & Hong, D. Fleximo: A flexible remote sensing foundation model (2025). URL <https://arxiv.org/abs/2503.23844>. [2503.23844](https://arxiv.org/abs/2503.23844).
- [197] Wu, K. *et al.* A semantic-enhanced multi-modal remote sensing foundation model for earth observation. *Nature Machine Intelligence* 1–15 (2025).
- [198] Bi, H. *et al.* Ringmoe: Mixture-of-modality-experts multi-modal foundation models for universal remote sensing image interpretation (2025). URL <https://arxiv.org/abs/2504.03166>. [2504.03166](https://arxiv.org/abs/2504.03166).